Karlsruhe Institute of Technology

2D ELASTIC FULL-WAVEFORM INVERSION OF LOVE WAVES IN VERTICALLY TRANSVERSELY ISOTROPIC MEDIA

2D ELASTISCHE WELLENFORMINVERSION VON LOVE WELLEN IN VERTIKAL TRANSVERSAL ISOTROPEN MEDIEN

Master's Thesis of

Valérie Krampe

KIT - Department of Physics
Geophysical Institute (GPI)

Reviewer:	Prof. Dr. Thomas Bohlen
Second Reviewer:	apl. Prof. Dr. Joachim Ritter

26. September 2018

I declare that I have developed and written the enclosed thesis completely by myself, and have not used sources or means without declaration in the text.

Karlsruhe, September 26, 2018, _____

Valérie Krampe

Abstract

In most shallow-seismic FWI studies, an isotropic approximation of the subsurface is used, even if most Earth materials are at least weakly anisotropic. We assume that for shallow sediments, a vertically transversely isotropic (VTI) approximation is more suitable due to the fine horizontal layering of the sediments. We investigate in this work the effects of this kind of anisotropy on surface waves and shallow-seismic FWI. The comparison of seismograms calculated in isotropic and VTI models shows that the sensitivity towards anisotropy is significantly higher for Love waves compared to Rayleigh waves. Therefore, we implemented the 2D anisotropic FWI only for SH waves. In synthetic examples, we investigate the capabilities of the VTI FWI. An almost perfect reconstruction of both horizontal and vertical velocities is possible, even if structures in the parameter models are spatially uncorrelated. To analyze the performance of VTI FWI also for a realistic case, we acquired field data at a site where the subsurface contains a highly anisotropic shale layer and applied the FWI to this data. In this case, it was not possible to reconstruct the anisotropy of the subsurface properly with the VTI FWI, mainly because of the strong velocity contrast between the shale and the overlying sediments. Further studies are necessary to develop methods that can handle such high velocity contrasts. Additionally, to prove the applicability and the use of the VTI FWI in shallow seismics, the method needs to be tested on further data sets.

Zusammenfassung

Obwohl die meisten Gesteine und Sedimentschichten anisotrope Eigenschaften aufweisen, wird bei Wellenforminversionen von Oberflächenwellen der Untergrund meist als isotrop angenommen. Aufgrund der horizontalen Schichtung von Sedimenten sollte die Annahme einer vertikal transversal isotropen (VTI) Struktur allerdings eine bessere Näherung darstellen. Wir untersuchen daher in dieser Arbeit die Auswirkungen dieser Art von Anisotropie auf Oberflächenwellen und auf deren Wellenforminversion. Der Vergleich von Seismogrammen, welche in isotropen und VTI Modellen berechnet wurden, zeigt, dass Love Wellen im Vergleich zu Rayleigh Wellen eine deutlich stärkere Sensitivität bezüglich Anisotropie aufweisen. Daher haben wir die 2D anisotrope Wellenforminversion vorerst nur für SH Wellen implementiert. In synthetischen Tests zeigen wir die Fähigkeiten der VTI Wellenforminversion. Es können sowohl die horizontalen als auch die vertikalen Geschwindigkeiten nahezu perfekt rekonstruiert werden, selbst wenn diese unterschiedliche räumliche Strukturen aufweisen. Um die Inversion auch an echten Daten zu testen, wurde eine Messung oberhalb einer stark anisotropen Schieferschicht durchgeführt. Es war nicht möglich, die Anisotropie dieses Schiefers mit der Wellenforminversion zu rekonstruieren, hauptsächlich aufgrund des hohen Geschwindigkeitskontrastes zwischen dem Schiefer und den darüber liegenden Sedimenten. Weitere Untersuchungen sind notwendig, um Methoden zu entwickeln, die eine erfolgreiche Inversion in einer solchen Umgebung ermöglichen. Um eine generelle Aussage über die Anwendbarkeit und den Nutzen der anisotropen Wellenforminversion von Oberflächenwellen machen zu können, müsste die Methode außerdem noch an weiteren Datensätzen getestet werden.

Contents

1. Introduction

With shallow-seismic methods, it is possible to obtain from surface waves information about the seismic velocities in the first few meters of the subsurface. Since surface waves are most sensitive to the shear-wave velocity, the focus of shallow-seismic methods lies on the reconstruction of this parameter. It has a great importance for geotechnical site characterization, since the shear-wave velocity of the first 30 m, v_s^{30}, is often used as parameter for soil classification and for seismic microzonation (Dobry et al., 2000).

Conventional methods for the analysis of surface waves are mainly based on the dispersive behavior of those waves (Socco et al., 2010). Since the depth of penetration of surface waves is dependent of the wavelength, it is possible to get from the frequency-dependent phase velocities, the dispersion curves, information about the velocity structure of the subsurface. The analysis and inversion of dispersion curves is a widely used shallow-seismic method to retrieve v_s models (Park et al., 1999; Xia et al., 1999; Xia, 2014). Unfortunately, this method only allows the generation of one-dimensional velocity models. Information about lateral variations of the subsurface can not be retrieved directly from the dispersion curves. A 2D or 3D model can only be created by a combination of the results from different profiles or from different source-receiver combinations together to one model, which will only have a limited lateral resolution (Bohlen et al., 2004).
With full-waveform inversion (FWI), it is possible to retrieve from seismic data 2D or even 3D models with a resolution of less than one wavelength and thus with a much higher resolution than with the classical methods. FWI, which was first proposed by Tarantola (1984), uses the whole information content of the data. The resulting model should thus be able to explain the complete waveform including phases and amplitudes of the recorded seismograms and not only onset times as it is the case e.g. for traveltime tomography. Obviously, this necessitates large computational resources, which is the main limitation factor for the application of FWI. However, with the growing capabilities of high-performance computing, FWI can today already be applied to large data sets in exploration seismics (Brossier et al., 2009; Sears et al., 2010; Prieux et al., 2013). The advantages of FWI also lead to an increasing use of this method for near-surface investigations. Despite the improvements made in the past years, the application of FWI to field data is still very challenging. Examples for field data applications in shallow seismics are given e.g. by Tran et al. (2013) and Groos et al. (2017). Most of shallow-seismic studies make only use of the Rayleigh waves, applications of FWI to Love waves as done by Dokter et al. (2017) or Pan et al. (2016) are in comparison quite rare. However, the use of SH data also has its advantages. Since the P-wave velocity has no effect on this component, there is one less parameter we have to invert for. This reduces the ambiguity of the inverse problem and also the computational time. We therefore focus in this work on the inversion of SH data.
Since the computational costs of FWI are extremely high even for acoustic or elastic simulations, the subsurface is in most studies assumed to be isotropic to avoid additional parameters needed to describe anisotropy. While in exploration seismics, the consideration of anisotropy in FWI gains more and more in importance (Prieux et al., 2011; Warner et al., 2013), it is still mostly ignored in shallow-seismic FWI, even if it is known that most earth materials are at least weakly anisotropic. The effects of anisotropy on surface waves and on shallow-seismic FWI are thus not known in detail yet.

Therefore, we investigate in this work the effects of the most common sort of anisotropy occuring in shallow sediments, the vertical transverse isotropy (VTI). We first implement a finite-difference simulation to calculate the wave propagation in VTI media. With this forward solver, we investigate the effects of anisotropy on surface waves by comparing the waveforms generated in VTI and isotropic models (chapter 3). This analysis gives us information about the sensitivity of Rayleigh and Love waves towards the different parameters that define anisotropy. Based on the results of this sensitivity tests, we implement and apply the anisotropic FWI only for Love waves. In the fourth chapter, we test the anisotropic FWI on synthetic data to explore the capabilities and limitations of the inversion. Finally, in the fifth chapter, we show a first application of the VTI inversion to field data that we acquired for this purpose.

2. Theoretical background

2.1. Seismic anisotropy

Anisotropy in general signifies that the properties of a material change with the direction in which they are measured. In the field of seismics, the relevant properties are the velocities of wave propagation, so that seismic anisotropy refers to the angle-dependency of wave velocities. In isotropic materials, the velocities of P- and S-waves are independent of the direction of wave propagation. On the contrary, in the case of seismic anisotropy, the velocity of wave propagation depends on the angle of propagation, so that waves are for example traveling faster in horizontal than in vertical direction. Anisotropy may be caused by many effects on different scales, so that most Earth materials show some sort of anisotropy. We distinguish between intrinsic and extrinsic or apparent anisotropy (Schön, 2015). Intrinsic anisotropy is caused by the preferred orientation of crystals or grains. This alignment can be created by flows of material, as it is the case in the upper mantle: Here, the olivine crystals are aligned in direction of the mantle flow, which creates a large-scale anisotropic structure. On larger scales than the crystalline scale, other mechanisms can lead to non-intrinsic anisotropy. An example therefor is the parallel alignment of cracks or pores in solid rocks due to the orientation of the stress field (Babuska and Cara, 1991).

In shallow depths, seismic anisotropy is mostly caused by sedimentation, which creates a horizontal layered structure. If the thickness of the layers is significantly smaller than the wavelength of propagated waves, this material will be seen as a homogeneous, but anisotropic medium (Backus, 1962). Even if the material of the layers itself is isotropic, the thin layering creates an apparently anisotropic structure. Because of the lateral homogeneity of the layers, the velocity of wave propagation depends only on the angle in the vertical plane and not on the horizontal angle. This symmetric form of anisotropy with a vertical axis of symmetry is called vertical transverse isotropy (VTI, see figure 2.1). If the axis of symmetry is not vertical but rotated in a certain angle, the material is no longer called vertical transversely isotropic, but tilted transversely isotropic (TTI) or horizontal transversely isotropic (HTI) for a horizontal orientation of the axis of symmetry. However, because of its simplicity and since this sort of structure is the most common in shallow depths, we consider in this work only VTI media.

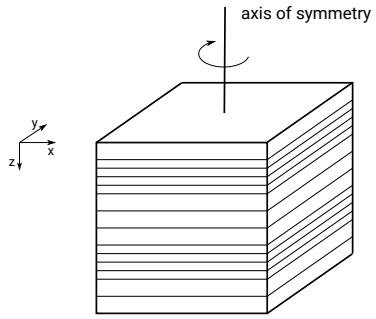

Figure 2.1.: Schematic illustration of a medium with vertical transverse isotropy (VTI) caused by layering

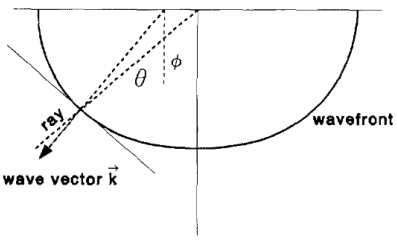

Figure 2.2.: Definition of the phase angle θ used in equations (2.1) - (2.3) and of the group angle ϕ (Thomsen, 1986)

For VTI media, the seismic anisotropy is usually defined by the Thomsen parameters ε, δ and γ, which define the angle-dependency of phase velocities for weak anisotropy as follows (Thomsen, 1986):

$$v_P(\theta) = v_{p,ver}\left(1 + \delta \sin^2\theta \cos^2\theta + \varepsilon \sin^4\theta\right) \tag{2.1}$$

$$v_{SV}(\theta) = v_{s,ver}\left(1 + \frac{v_{P,ver}^2}{v_{S,ver}^2}(\varepsilon - \delta)\sin^2\theta\cos^2\theta\right) \tag{2.2}$$

$$v_{SH}(\theta) = v_{s,ver}\left(1 + \gamma \sin^2\theta\right) \tag{2.3}$$

In these equations, the so-called phase angle θ corresponds to the angle between the vertical axis and the normal of the wavefront, which is in the anisotropic case not equal to the group angle, the angle between vertical axis and ray direction (see figure 2.2). As we can see from the equations, the velocities of P- and SV-waves depend on a combination of ε and δ, while the velocity of SH-waves v_{SH} is only affected by γ. The values of the three Thomsen parameters are normally in the same order of magnitude, typical values for sedimentary rocks are in the range between 0.01 and 0.3. The parameters can also be negative, for example a negative value of γ would mean that the velocity of SH-waves is higher in vertical than in horizontal direction.

To visualize the effects of anisotropy on the velocities, we show in figure 2.3 the angle-dependency of the velocities after equations (2.1) - (2.3) for angles from 0° (vertical propagation) up to 90° (horizontal propagation). We chose the Thomsen parameters $\varepsilon = 0.110$, $\delta = -0.035$ and $\gamma = 0.255$, and as vertical velocities we use $v_p = 3300\,\frac{\mathrm{m}}{\mathrm{s}}$ and $v_s = 1800\,\frac{\mathrm{m}}{\mathrm{s}}$. The chosen values are based on values for sandstone given by Thomsen (1986). As we can see in figure 2.3, the general shape of angle-dependency is different for SV- and SH-waves. For SV-waves, horizontal and vertical velocities are equal to each other regardless of the values of the Thomsen parameters, while for SH waves their difference is proportional to γ. This has the effect that for positive Thomsen parameters, the SV-wave reaches its maximal velocity at an angle of 45° and not like the SH wave at 90°. The shape of the P-wave curve is similar to the SH curve, the maximal P-wave velocity is also reached for a horizontal direction of propagation. For small angles, v_p is even smaller than for vertical direction, this effect is caused by the negative δ-value. As we will show later, the different angle-dependencies of P-, SV- and SH-waves have an influence on the sensitivity of Rayleigh and Love waves towards anisotropy.

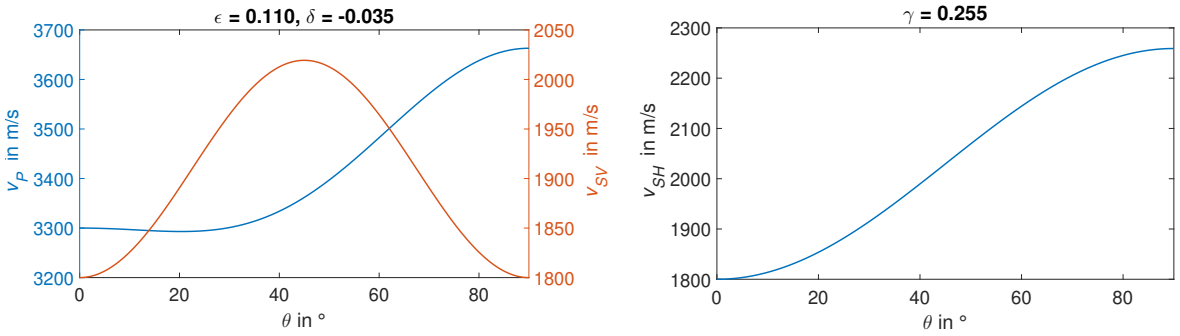

Figure 2.3.: Dependency from the phase angle θ of velocities of P- and SV-waves with $\varepsilon = 0.110$ and $\delta = -0.035$ (left) and of SH waves with $\gamma = 0.255$ (right)

2.2. Forward modeling

A main part of each FWI software is the forward solver that calculates the propagation of a wavefield in a given model. In this section, we introduce the equations that are necessary to calculate the wave propagation in VTI media for the elastic case as well as for the viscoelastic case. Additionally, we explain some details about the numerical implementation of those equations, which is done with the finite-difference method.

2.2.1. Elastic equations

In elastic media, the relation between the components of the stress tensor σ and the strain tensor ε is given by Hooke's law, that is

$$\sigma_{ij} = c_{ijkl}\varepsilon_{kl}, \tag{2.4}$$

where c_{ijkl} are the components of the stiffness tensor $\mathbf{c}$. The components of the strain tensor are given by

$$\varepsilon_{kl} = \frac{1}{2}\left(\frac{\partial u_k}{\partial x_l} + \frac{\partial u_l}{\partial x_k}\right) \tag{2.5}$$

with the displacement vector $\vec{u}$.

In the general case of anisotropy, the stiffness tensor consists of 21 independent components due to the symmetry of stress and strain tensors and the invariants of a tensor. Therefore, the tensor can be written as a 6 x 6 matrix by reducing the four indices to only two. This is done by transforming the indices i, j to m and k, l to n in the following way:
$11 \rightarrow 1$, $22 \rightarrow 2$, $33 \rightarrow 3$, $23 \rightarrow 4$, $13 \rightarrow 5$, $12 \rightarrow 6$
The Hooke's law can now be written as

$$\sigma_m = c_{mn}\varepsilon_n \tag{2.6}$$

In transversely isotropic materials, $\mathbf{c}$ consists only of 12 components (Thomsen, 1986):

$$\mathbf{c} = \begin{pmatrix} c_{11} & c_{12} & c_{13} & 0 & 0 & 0 \\ c_{12} & c_{22} & c_{23} & 0 & 0 & 0 \\ c_{13} & c_{23} & c_{33} & 0 & 0 & 0 \\ 0 & 0 & 0 & c_{44} & 0 & 0 \\ 0 & 0 & 0 & 0 & c_{55} & 0 \\ 0 & 0 & 0 & 0 & 0 & c_{66} \end{pmatrix} \tag{2.7}$$

From those twelve components, only five are independent. For a vertical axis of symmetry (VTI), we have the following relations between the elastic constants:

$$\begin{aligned} c_{22} &= c_{11} \\ c_{44} &= c_{55} \\ c_{23} &= c_{13} \\ c_{12} &= c_{11} - 2c_{66} \end{aligned} \tag{2.8}$$

In this work, the axis x, y and z of the coordinate system are defined in a way that x is the 1-axis, y the 2-axis and z the 3-axis (vertical).

To get a relation between stress and velocity, we use the derivative of equation (2.4), that is

$$\dot{\sigma}_{ij} = c_{ijkl}\dot{\varepsilon}_{kl}, \tag{2.9}$$

where $\dot{\varepsilon}_{kl}$ is given by

$$\dot{\varepsilon}_{kl} = \frac{1}{2}\left(\frac{\partial v_k}{\partial x_l} + \frac{\partial v_l}{\partial x_k}\right). \tag{2.10}$$

Additionally, we use Newton's law

$$\rho \dot{v}_i = \frac{\partial \sigma_{ij}}{\partial x_j}. \tag{2.11}$$

Equations (2.9) and (2.11) are finally leading to a system of first-order differential equations with velocity and stress components as variables. In two dimensions, where all partial derivatives with respect to y are zero, the system consists of the following equations:

P/SV waves

$$\rho \dot{v}_x = \frac{\partial \sigma_{xx}}{\partial x} + \frac{\partial \sigma_{xz}}{\partial z} \tag{2.12}$$

$$\rho \dot{v}_z = \frac{\partial \sigma_{xz}}{\partial x} + \frac{\partial \sigma_{zz}}{\partial z} \tag{2.13}$$

$$\dot{\sigma}_{xx} = c_{11}\frac{\partial v_x}{\partial x} + c_{13}\frac{\partial v_z}{\partial z} \tag{2.14}$$

$$\dot{\sigma}_{zz} = c_{13}\frac{\partial v_x}{\partial x} + c_{33}\frac{\partial v_z}{\partial z} \tag{2.15}$$

$$\dot{\sigma}_{xz} = c_{55}\left(\frac{\partial v_x}{\partial z} + \frac{\partial v_z}{\partial x}\right) \tag{2.16}$$

SH waves

$$\rho \dot{v}_y = \frac{\partial \sigma_{xy}}{\partial x} + \frac{\partial \sigma_{yz}}{\partial z} \tag{2.17}$$

$$\dot{\sigma}_{xy} = c_{66}\frac{\partial v_y}{\partial x} \tag{2.18}$$

$$\dot{\sigma}_{yz} = c_{55}\frac{\partial v_y}{\partial z} \tag{2.19}$$

With those equations, it is possible to calculate the velocity and stress values of the wavefield numerically if the elastic constants $c_{11}, c_{13}, c_{33}, c_{55}, c_{66}$ and the density ρ are known for the whole model. The equation for $\dot{\sigma}_{yy}$ is not needed for the 2D case. As we can see in equations (2.12) - (2.19), the equations for P/SV-waves and for SH-waves are for a 2D VTI medium completely decoupled. The stress equations can be written in matrix notation, which will be helpful for the derivation of the gradients for FWI. In the following, we will use for the spatial derivatives of the velocities the notation $\frac{\partial v_x}{\partial y} = v_{x,y}$. The two resulting matrix equations for P-/SV-waves and SH-waves, respectively, are then

$$\begin{pmatrix} \dot{\sigma}_{xx} \\ \dot{\sigma}_{zz} \\ \dot{\sigma}_{xz} \end{pmatrix} = \begin{pmatrix} c_{11} & c_{13} & 0 \\ c_{13} & c_{33} & 0 \\ 0 & 0 & c_{55} \end{pmatrix} \begin{pmatrix} v_{x,x} \\ v_{z,z} \\ v_{x,z} + v_{z,x} \end{pmatrix} \tag{2.20}$$

and

$$\begin{pmatrix} \dot{\sigma}_{xy} \\ \dot{\sigma}_{yz} \end{pmatrix} = \begin{pmatrix} c_{66} & 0 \\ 0 & c_{55} \end{pmatrix} \begin{pmatrix} v_{y,x} \\ v_{y,z} \end{pmatrix}. \tag{2.21}$$

2.2.2. Viscoelastic equations

When working with field data, it is necessary to consider the attenuation of seismic waves at least in the forward modeling part of FWI. Seismic attenuation is usually defined by the quality factor $Q = 2\pi\frac{E}{\Delta E}$ with ΔE being the energy loss per cycle. In viscoelastic media, the stress components are not related to the strain by multiplication with the stiffness tensor $\mathbf{c}$ as in equation (2.4), but by convolution, so that

$$\sigma_{ij} = c_{ijkl} * \varepsilon_{kl} \tag{2.22}$$

(Christensen, 1982). The attenuation of real media can be approximated by a rheological model called the generalized standard linear solid (GSLS, Liu et al. (1976)), which consists of a certain number of Maxwell bodies connected parallel to a spring. Each Maxwell body represents a

relaxation mechanism and has a given relaxation frequency f_l, from which the relaxation time $\tau_{\sigma,l} = \frac{1}{2\pi f_l}$ can be calculated. By adjusting the number and the properties of relaxation mechanisms, the frequency dependency of Q can be defined in a way that the real attenuation is simulated as good as possible.

Following the derivations of Bohlen (2002) and Carcione et al. (1988), we obtain for one single relaxation mechanism the following viscoelastic equations of motion for SH waves:

$$\rho \dot{v}_y = \frac{\partial \sigma_{xy}}{\partial x} + \frac{\partial \sigma_{yz}}{\partial z} \tag{2.23}$$

$$\dot{\sigma}_{xy} = c_{66}(1+\tau)\frac{\partial v_y}{\partial x} + r_{xy} \tag{2.24}$$

$$\dot{\sigma}_{yz} = c_{55}(1+\tau)\frac{\partial v_y}{\partial z} + r_{yz} \tag{2.25}$$

$$\dot{r}_{xy} = -\frac{1}{\tau_\sigma}\left(c_{66}\tau\frac{\partial v_y}{\partial x} + r_{xy}\right) \tag{2.26}$$

$$\dot{r}_{yz} = -\frac{1}{\tau_\sigma}\left(c_{55}\tau\frac{\partial v_y}{\partial z} + r_{yz}\right) \tag{2.27}$$

Here, r_{xy} and r_{yz} are memory variables used to avoid the calculation of the convolution in (2.22) as proposed by Robertsson et al. (1994) and Carcione et al. (1988). The parameter τ defines the strength of attenuation and can be estimated with $\tau = 2/Q$ from a given Q-model. As relaxation frequency of a single Maxwell body, the main frequency of the source signal can be used, from which the relaxation time τ_σ can be calculated.

2.2.3. Numerical implementation

For simple models as for example a homogeneous velocity model, it is possible to solve the wave equations (2.12) - (2.19) analytically. However, the subsurface normally has a more complex structure, so that it is necessary to solve those equations numerically to calculate the wave propagation. In the software IFOS2D that is used for this work, the calculation of wave propagation is done with the finite-difference (FD) method. For this method, space and time have to be discretized, so that the partial derivatives in the wave equations can be approximated by finite-difference operators.

Discretization

The space domain is discretized by equidistant grid points with a grid spacing of Δh both in x- and z-direction. The coordinates of the grid points are given by $x = i\Delta h$ and $z = j\Delta h$, where i and j denote the number of a specific grid point.
The time domain is discretized similarly with a constant time spacing Δt, so that the time at the n-th timestep is given by $t = n\Delta t$.

In this work, a discretization on a staggered grid is used (Virieux, 1986; Levander, 1988). This means that different parameters are defined on different grids which are shifted against each other by $\frac{1}{2}\Delta h$. Figure 2.4 shows which parameters are defined on which grid points. The model parameters, i.e. the density and the elastic constants, are always defined on full grid points, while the stress and velocity components and the memory variables are distributed on the four different grids.
To calculate stresses and velocities, the spatial and temporal derivatives in the wave equations are replaced by finite-difference operators. As example, the derivatives of a function $f(x,t)$ at

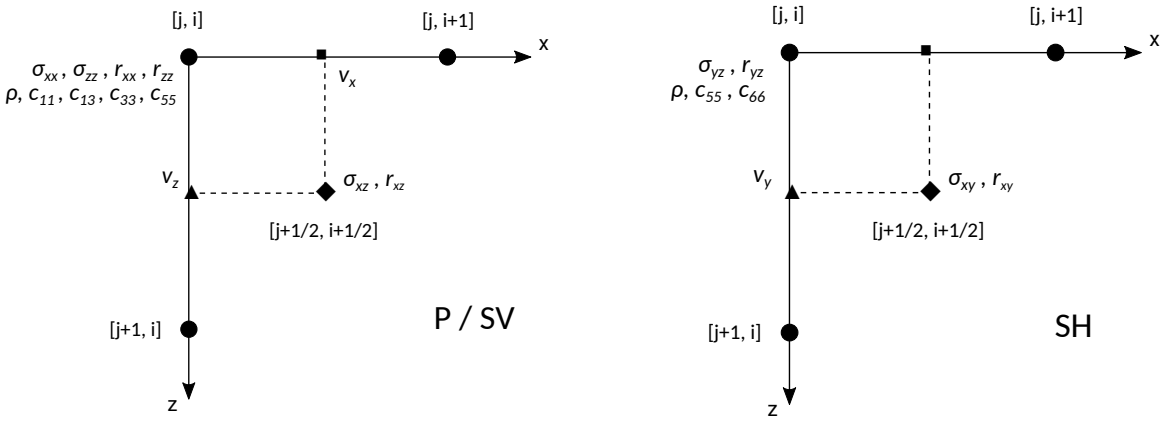

Figure 2.4.: Distribution of parameters on a standard staggered grid for P-/SV-waves (left) and SH-waves (right), after Virieux (1984, 1986).

the i-th grid point and at the n-th time step are approximated in a second-order approximation by

$$\frac{\partial f}{\partial x}[n,i] = \frac{f[n,i+1/2] - f[n,i-1/2]}{\Delta h} \tag{2.28}$$

$$\frac{\partial f}{\partial t}[n,i] = \frac{f[n+1/2,i] - f[n-1/2,i]}{\Delta t} \tag{2.29}$$

Operators of a higher order include more than only the neighbouring grid points and assure thus a higher accuracy. In this work, we use second-order approximations in time and sixth-order approximations in space. The choice of the higher-order operator in space allows us to use a wider grid spacing and reduces thus the total number of grid points.

Since for the calculation of stress and velocity components, the model parameters ρ and c_{ij} have to be defined at the correspondent grid points, it is necessary to average them from the given values at the full grid points. The density is needed for all velocity components and is averaged arithmetically, so that the values at the gridpoints of the velocities are calculated as

$$\rho[j,i+\frac{1}{2}] = \frac{1}{2}\left(\rho[j,i] + \rho[j,i+1]\right) \ , \tag{2.30}$$

$$\rho[j+\frac{1}{2},i] = \frac{1}{2}\left(\rho[j,i] + \rho[j+1,i]\right) \ . \tag{2.31}$$

From the elastic constants, only c_{55} for the P/SV case and c_{66} for the SH case have to be averaged to calculate the stress components σ_{xz} and σ_{xy}. In contrast to the density, those have to be averaged harmonically (Moczo et al., 2004), and the four values surrounding the grid point $[j+\frac{1}{2}, i+\frac{1}{2}]$ are used, so that the averaged parameters are calculated as

$$c_{ii}[j+\frac{1}{2},i+\frac{1}{2}] = \left[\frac{1}{4}\left(\frac{1}{c_{ii}}[j,i] + \frac{1}{c_{ii}}[j,i+1] + \frac{1}{c_{ii}}[j+1,i] + \frac{1}{c_{ii}}[j+1,i+1]\right)\right]^{-1} \ . \tag{2.32}$$

The approximation of the wave equations by the FD operators is shown here in an exemplary way for only one of the equations, namely equation (2.12). Replacing the partial derivatives by

the FD operators yields

$$\rho[j,i+\frac{1}{2}]\frac{v_x^{n+\frac{1}{2}}[j,i+\frac{1}{2}]-v_x^{n-\frac{1}{2}}[j,i+\frac{1}{2}]}{\Delta t}=\frac{\sigma_{xx}^n[j,i+1]-\sigma_{xx}^n[j,i]}{\Delta h}+\frac{\sigma_{xz}^n[j+\frac{1}{2},i+\frac{1}{2}]-\sigma_{xz}^n[j-\frac{1}{2},i+\frac{1}{2}]}{\Delta h} \tag{2.33}$$

In this equation, there is only one parameter at the future time step $n+\frac{1}{2}$. By rearranging equation (2.33), we can calculate it from the parameters at the actual and the last time step:

$$v_x^{n+\frac{1}{2}}[j,i+\frac{1}{2}]=v_x^{n-\frac{1}{2}}[j,i+\frac{1}{2}]+\frac{1}{\rho[j,i+\frac{1}{2}]}\ \frac{\Delta t}{\Delta h}\ (\ \sigma_{xx}^n[j,i+1]-\sigma_{xx}^n[j,i]+ \\ \sigma_{xz}^n[j+\frac{1}{2},i+\frac{1}{2}]-\sigma_{xz}^n[j-\frac{1}{2},i+\frac{1}{2}]\ ) \tag{2.34}$$

For the other wave equations, the FD approximation works in a similar way, from each equation results one future parameter that is calculated from the values at the actual and the previous time step.

Boundary conditions

For a realistic forward modeling, we have to implement a stress-free surface and absorbing boundaries on the other three edges of the model. The absorbing boundaries are implemented with the method of Perfectly Matched Layers (PML) after Komatitsch and Martin (2007).
The free surface is realized by the mirroring technique proposed by Levander (1988). All vertical stresses at the grid points where the free surface is located are set to $\sigma_{xz}=\sigma_{zz}=\sigma_{yz}=0$. The stresses above the free surface are calculated by mirroring the values below the surface with an inverse sign. When calculating the remaining stress components, it should be avoided for reasons of stability to use vertical derivatives of the velocities, which matters only for σ_{xx}. Therefore, we replace $v_{z,z}$ in the calculation of σ_{xx} by using equation (2.15):

$$\sigma_{zz}=\Delta t\ (c_{13}v_{x,x}+c_{33}v_{z,z})=0 \tag{2.35}$$

$$\Rightarrow \quad v_{z,z}=-\frac{c_{13}}{c_{33}}v_{x,x} \tag{2.36}$$

In each iteration step, it is thus necessary to undo the last update of σ_{xx} (which is calculated before with equation (2.14)), and to add the correct update for the free surface. The final equation for σ_{xx} at the n-th timestep thus is

$$\sigma_{xx}^n=\sigma_{xx}^{n-1}+\Delta t\ (c_{11}-\frac{c_{13}^2}{c_{33}})v_{x,x}. \tag{2.37}$$

Numerical stability

To guarantee the numerical stability of the FD-calculation, the time spacing Δt has to be smaller than a certain value defined by the Courant-Friedrichs-Lewy criterion (Courant et al., 1967). This condition assures that the wave is not propagating further than to the adjacent grid points in one time step. The maximal value for Δt is given for the 2D case by

$$\Delta t\leq\frac{\Delta h}{h\sqrt{2}v_{max}} \tag{2.38}$$

where h is the sum of the weighting coefficients of the FD operator and thus depends on the FD order.

Additionally, to avoid numerical grid dispersion, which depends on the number of grid points per wavelength, the grid spacing Δh should fulfill the condition

$$\Delta h \leq \frac{\lambda_{min}}{n} = \frac{v_{min}}{n f_{max}} \tag{2.39}$$

Here, n denotes the necessary number of grid points per wavelength and depends on the FD-order, e.g. $n = 12$ for a FD-order of 2.

2.3. Full-waveform inversion

2.3.1. Inversion method

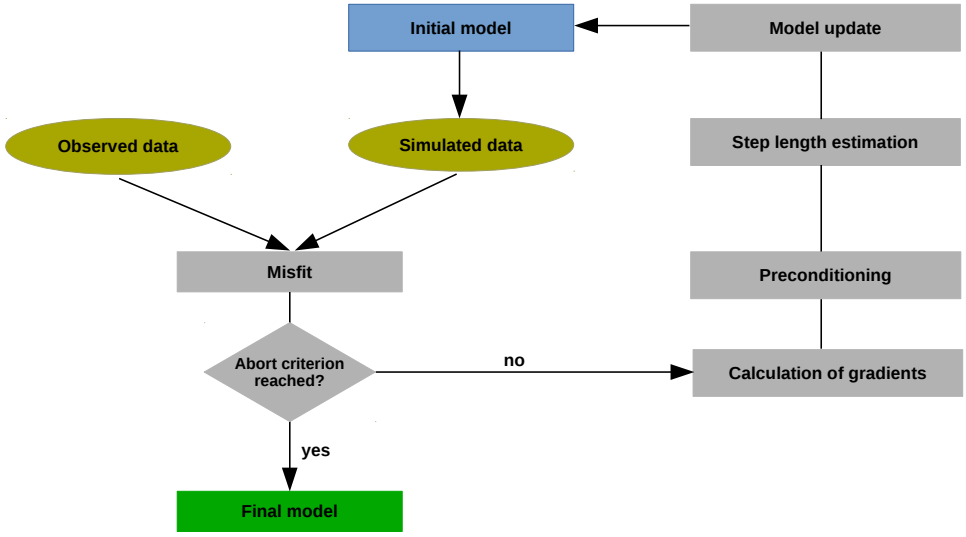

Figure 2.5.: Schematic visualization of the iterative FWI process.

The aim of all inverse methods in seismics is to retrieve from the observed data information about the subsurface in which the seismic waves are propagating. In classical methods as for example traveltime tomography, only the information about the onset times of different phases is used and the result of the inversion will be a subsurface model that can explain the travel times of those phases. All other information available in the data as amplitudes and the waveform is not used. With full-waveform inversion, all information content of the data is used for the inversion, so that the resulting inverted model should be able to explain the complete recorded seismograms. Obviously, this method is correlated with much higher computational costs than traveltime based methods, which is one of the greatest challenges of FWI.

Full-waveform inversion was first developed by Tarantola (1984), and most of the further developments and applications are based on this work. A good overview of the current state of the art of FWI is given e.g. in Virieux and Operto (2009), a more detailed description can be found in Fichtner (2011). In this section, only the basic principle of FWI and details concerning the implementation of a VTI FWI are explained.

The basic principle of FWI is shown in figure 2.5. At the beginning, the observed data is

compared with numerically calculated data from a synthetic initial model, which should be in the ideal case not too far away from the true model. Therefore, all available a-priori information about the site should be used to create an appropriate initial model. The misfit between observed and synthetic data is defined by a certain objective function $J(m)$ which can be for example the L2 norm. This misfit is then minimized within an iterative process. In each iteration, variations δm of the model parameters are calculated so that the data resulting from the new model fits better the observed data. The calculation of model updates is based on the steepest descent method, the new model parameters are defined through the parameters of the previous iteration as

$$m_{n+1} = m_n - \alpha_n P_n \left(\frac{\partial J}{\partial m} \right)_n \ . \tag{2.40}$$

Here, P denotes a preconditioning matrix and α the step length. The gradient of the misfit function defines the direction of the change of the model parameters, and the step length defines how much the model parameters are allowed to change in one iteration and thus has a high influence on the number of iterations. If α is chosen too small, only small changes of model parameters are applied in each step, so that many iterations are necessary to reduce the misfit. On the other hand, if the step length is chosen too big, it can happen that the minimum of the objective function is missed so that the best model can not be found. To find an appropriate step length, in each iteration a parabolic step length search is used. Therefore, for a few shots the misfit is calculated for three different step length and the misfit values are fitted with a parabolic curve. The step length at which this curve has its minimum is then used as step length for the actual iteration.

To increase the speed of convergence, in our inversion software IFOS2D the preconditioned conjugate gradient method (PCG) is used (Nocedal and Wright, 2006). In this method, not only the actual gradient ∇J_n is used to calculate the model updates, but also the gradient from the previous iteration, so that the updates are calculated via

$$\delta m_n = -P_n \nabla J_n + \beta_n \delta m_{n-1} \ . \tag{2.41}$$

There are different possibilities how the factor β_n is defined, e.g. as proposed by Hestenes and Stiefel (1952) or Fletcher and Reeves (1964). We use the definition after Polak and Ribière (1969), that is

$$\beta_n = \frac{\nabla J_n^T (\nabla J_n - \nabla J_{n-1})}{||\nabla J_n||^2} \ . \tag{2.42}$$

As preconditioning matrix P, we use an energy preconditioning as proposed by Plessix and Mulder (2004). The calculation of the gradients will be explained in the following section.

2.3.2. Calculation of gradients

To calculate the gradients of the objective function J that are needed for the model updates, we use the method of Lagrange multipliers, which is a mathematical method for solving constrained optimization problems. The following derivation is based on the descriptions in Plessix (2006) and Liu and Tromp (2006). We derive here only the gradients for the SH component, since we will invert in this work only this component.

In FWI, we want to minimize the objective function that could be for example the L2 norm of observed and synthetic velocities:

$$J(m) = \frac{1}{2} \sum_r \sum_i \int_0^T (v_i - v_{obs,i})^2 \ dt \tag{2.43}$$

Here, v_i are the components of particle velocity calculated numerically in the actual model, and $v_{obs,i}$ are the velocities from the observed seismograms. The summation over r indicates the summation over all receivers. The constraints that have to be fulfilled are the two equations of the velocity-stress formulation of the wave equation

$$\rho \dot{v}_i = \frac{\partial \sigma_{ij}}{\partial x_j} + f_i \tag{2.44}$$

$$\dot{\sigma}_{ij} = c_{ijkl} \frac{\partial v_k}{\partial x_l} \tag{2.45}$$

with the initial conditions $v_i(t=0) = 0$ and $\sigma_{ij}(t=0) = 0$.

We now want to minimize the objective function (2.43) under the constraints (2.44) and (2.45). Therefore, we construct the augmented Langrangian $\mathcal{L}$ by multiplying the constraints with the Lagrange multipliers ψ_i^1 and ψ_{ij}^2 and subtract them from the function we want to minimize, yielding

$$\begin{aligned} \mathcal{L} = \frac{1}{2} \sum_r \sum_i \int_0^T (v_i - v_{obs,i})^2 \, dt - \iint d\Omega dt \; \psi_i^1 (\rho \dot{v}_i - \frac{\partial \sigma_{ij}}{\partial x_j} - f_i) \\ - \iint d\Omega dt \; \psi_{ij}^2 (\dot{\sigma}_{ij} - c_{ijkl} \frac{\partial v_k}{\partial x_l}) \end{aligned} \tag{2.46}$$

where $\int d\Omega$ denotes the integration over the complete volume.
Following the theory of the method of Lagrange multipliers, all derivatives of $\mathcal{L}$ with respect to the parameters v_i, σ_{ij} and to the Lagrange multipliers ψ_i^1, ψ_{ij}^2 have to be zero. To calculate the derivatives with respect to v_i and σ_{ij}, we have to partially integrate equation (2.46) in space and time, resulting in

$$\begin{aligned} \mathcal{L} = \frac{1}{2} \sum_r \sum_i \int_0^T (v_i - v_{obs,i})^2 \, dt + \iint d\Omega dt \; (\rho \dot{\psi}_i^1 v_i - \frac{\partial \psi_i^1}{\partial x_j} \sigma_{ij} + \psi_i^1 f_i) \\ + \iint d\Omega dt \; (\dot{\psi}_{ij}^2 \sigma_{ij} - \frac{\partial \psi_{ij}^2 c_{ijkl}}{\partial x_l} v_k) \; . \end{aligned} \tag{2.47}$$

The terms evaluated at the bounds that result from the integration by parts are zero and therefore do not appear in this equation. However, from those terms do the boundary conditions $\psi_i^1(T) = 0$ and $\psi_{ij}^2(T) = 0$ result. Additionally, we use the boundary conditions that all wavefields are zero at the space boundary $\delta\Omega$.

The derivation of equation (2.47) yields

$$\frac{\partial \mathcal{L}}{\partial v_i} = 0 \quad \Leftrightarrow \quad \rho \dot{\psi}_i^1 = \frac{\partial \psi_{kl}^2 c_{klij}}{\partial x_j} - (v_i - v_{obs,i}) \tag{2.48}$$

$$\frac{\partial \mathcal{L}}{\partial \sigma_{ij}} = 0 \quad \Leftrightarrow \quad \dot{\psi}_{ij}^2 = \frac{\partial \psi_i^1}{\partial x_j} \; . \tag{2.49}$$

Those equations look similar to the wave equations (2.44) and (2.45), but the initial conditions of ψ_i^1 and ψ_{ij}^2 are given at time $t = T$ but not at $t = 0$. To change this, we write the equations

reversed in time, i.e. we replace t with $T-t$ yielding

$$\rho\dot{\psi}_i^1(T-t) = \frac{\partial\psi_{kl}^2(T-t)c_{klij}}{\partial x_j} - (v_i - v_{obs,i})(T-t) \tag{2.50}$$

$$\dot{\psi}_{ij}^2(T-t) = \frac{\partial\psi_i^1(T-t)}{\partial x_j} \ . \tag{2.51}$$

We now substitute $T-t$ by τ, which yields because of $\dot{\psi}_i^1(T-t) = -\dot{\psi}_i^1(\tau)$

$$\rho\dot{\psi}_i^1(\tau) = -\frac{\partial\psi_{kl}^2(\tau)c_{klij}}{\partial x_j} + (v_i - v_{obs,i})(\tau) \tag{2.52}$$

$$\dot{\psi}_{ij}^2(\tau) = -\frac{\partial\psi_i^1(\tau)}{\partial x_j} \tag{2.53}$$

with $\psi_i^1(\tau=0) = 0$ and $\psi_{ij}^2(\tau=0) = 0$. To bring those equations to the same form as the wave equations, we now only have to replace the term $-c_{klij}\psi_{kl}^2$ with a new variable that we call $\tilde{\psi}_{ij}^2$. With this, the final equations are

$$\rho\dot{\psi}_i^1(\tau) = \frac{\partial\tilde{\psi}_{ij}^2(\tau)}{\partial x_j} + (v_{obs,i} - v_i)(\tau) \tag{2.54}$$

$$\dot{\tilde{\psi}}_{ij}^2(\tau) = c_{ijkl}\frac{\partial\psi_k^1(\tau)}{\partial x_l} \ . \tag{2.55}$$

Those equations are called the **adjoint equations**. Since τ corresponds to the reversed time t, the **adjoint wavefields** ψ_i^1 and $\tilde{\psi}_{ij}^2$ can be calculated by backpropagation of the **adjoint source**, which is defined for the L2 norm as residual between observed and synthetically calculated seismograms reversed in time. ψ_i^1 then corresponds to the backpropagated velocity field and will therefore be called from now on v_i^*, and $\tilde{\psi}_{ij}^2$ corresponds to the backpropagated stress field, called σ_{ij}^*.

The gradients of the objective function $J(m)$ with respect to the model parameters m are derived by equation (2.46), since $\frac{\partial J}{\partial m} = \frac{\partial\mathcal{L}}{\partial m}$. The resulting gradients are

$$\frac{\partial J}{\partial\rho} = -\int dt\ v_i^*\dot{v}_i \tag{2.56}$$

$$\frac{\partial J}{\partial c_{ijkl}} = \int dt\ \psi_{ij}^2\frac{v_k}{x_l} \ . \tag{2.57}$$

To calculate the second gradient, we have to replace ψ_{ij}^2 and $\frac{v_k}{x_l}$ by σ_{ij}^* and σ_{ij}, which can be done by calculating the inverse of the stiffness matrix $\mathbf{c}$. For SH-waves, rearranging of equation (2.21) yields

$$\begin{pmatrix} v_{y,x} \\ v_{y,z} \end{pmatrix} = \begin{pmatrix} 1/c_{66} & 0 \\ 0 & 1/c_{55} \end{pmatrix}\begin{pmatrix} \dot{\sigma}_{xy} \\ \dot{\sigma}_{yz} \end{pmatrix} \ . \tag{2.58}$$

Doing the same calculation for σ^*_{ij}, we get the final gradients

$$\frac{\partial J}{\partial c_{55}} = -\int dt\ \frac{1}{c^2_{55}}\dot{\sigma}_{yz}\sigma^*_{yz} \tag{2.59}$$

$$\frac{\partial J}{\partial c_{66}} = -\int dt\ \frac{1}{c^2_{66}}\dot{\sigma}_{xy}\sigma^*_{xy} \tag{2.60}$$

$$\frac{\partial J}{\partial \rho} = -\int dt\ v^*_y\dot{v}_y\ . \tag{2.61}$$

With those equations, it is possible to calculate the gradients by crosscorrelating the forward and adjoint wavefields. To get the adjoint wavefields, it is only necessary to backpropagate the residuals of velocity seismograms from the receiver positions.

2.3.3. Parameterization

Knowing the gradients with respect to the elements of the stiffness matrix c_{ijkl}, it is possible to calculate directly the gradients for different parameterizations, e.g. for vertical velocity and Thomsen parameter (ρ, $v_{s,ver}$, γ) or for horizontal and vertical velocities (ρ, $v_{s,ver}$, $v_{s,hor}$). Other studies showed that the choice of parameters has a high influence on the convergence of FWI. For isotropic FWI, it was for example shown by Köhn et al. (2012) that the parameterization with ρ, v_p and v_s is the most suitable. For FWI in VTI media, studies concerning the parameterization were carried out e.g. by Plessix and Cao (2011) for acoustic FWI and by Kamath et al. (2017) and Guitton and Alkhalifah (2017) for elastic FWI. In all those studies, only P/SV waves were considered, so that their results can not be applied to our case. In this work, we do not investigate the differences of the parameterizations further. We chose to invert for horizontal and vertical velocities, since their similar order of magnitude guarantees a higher stability of the inversion. Additionally, those parameters have the most intuitive physical meaning. The corresponding gradients are calculated by applying the chain rule on equations (2.59) - (2.61) and using the following relations (Thomsen, 1986):

$$c_{55} = \rho v^2_{s,ver} \tag{2.62}$$

$$c_{66} = \rho v^2_{s,hor} \tag{2.63}$$

Note that due to the different parameterization also the gradient with respect to ρ changes. Thus, the gradients used for the model updates are

$$\frac{\partial J}{\partial v_{s,ver}} = \frac{\partial J}{\partial c_{55}}\ 2\rho v_{s,ver}\ , \tag{2.64}$$

$$\frac{\partial J}{\partial v_{s,hor}} = \frac{\partial J}{\partial c_{66}}\ 2\rho v_{s,hor}\ , \tag{2.65}$$

$$\frac{\partial J}{\partial \rho'} = \frac{\partial J}{\partial c_{55}}\ v^2_{s,ver} + \frac{\partial J}{\partial c_{66}}\ v^2_{s,hor} + \frac{\partial J}{\partial \rho}\ . \tag{2.66}$$

3. Anisotropic forward modeling

3.1. Benchmark

We implemented the 2D anisotropic forward modeling for P/SV-waves and for SH-waves in the inversion software IFOS2D. To benchmark the forward solver, we compare the results with an analytical solution provided by Payton (1983). This analytical solution is only available for a homogeneous model and only for the P/SV components. Since the implementation of the SH component is similar, we assume that a correct implementation of the P/SV forward modeling also ensures a correct SH modeling. Additionally, we compare the results of the VTI forward solver with isotropic parameters ($\varepsilon = \delta = \gamma = 0$) to the results of the already existing isotropic forward solver for all components.

3.1.1. Comparison of VTI and isotropic forward solver

An isotropic medium can be seen as a special case of a VTI medium for which all Thomsen parameters are equal to zero. Therefore, in this case, the VTI forward simulation has to be consistent with the isotropic simulation. To verify this consistency, we compare for the same model the wavefields calculated with the already existing isotropic forward solver in IFOS2D with those calculated with the new VTI forward solver. The used model consists of a 5 m thick layer with $v_p = 300\,\frac{\mathrm{m}}{\mathrm{s}}$, $v_s = 150\,\frac{\mathrm{m}}{\mathrm{s}}$ and $\rho = 1800\,\frac{\mathrm{kg}}{\mathrm{m}^3}$ over a halfspace with $v_p = 500\,\frac{\mathrm{m}}{\mathrm{s}}$, $v_s = 300\,\frac{\mathrm{m}}{\mathrm{s}}$ and $\rho = 2000\,\frac{\mathrm{kg}}{\mathrm{m}^3}$. The source and receivers are located at the surface of the model, as source signal a Ricker wavelet with a center frequency of 50 Hz is used. The wave propagation is calculated for P/SV-waves and for SH-waves, so that all three components of the particle velocity can be compared. The vertical component v_z and the horizontal inline component v_x contain the P- and SV-waves and thus the Rayleigh waves, on the horizontal crossline component v_y only SH-waves and the Love wave appear. For all three components, we show the seismograms at different offsets for both simulations in figure 3.1. The waveforms of VTI and isotropic modeling are identical at every receiver and on each component, which proves the consistency of both forward solvers.

3.1.2. Comparison of numerical and analytical solution

The comparison of VTI and isotropic forward solver only assures that for the special case of a VTI medium with $\varepsilon = \delta = \gamma = 0$, which corresponds to an isotropic medium, the forward calculation is implemented correctly. To check whether it is also working properly for anisotropic media, we have to use a different reference than the isotropic solver. Payton (1983) provides an analytical solution for the location of the wavefronts in VTI media as well as for the waveform at receivers located along the axis of symmetry. We use those analytical solutions to validate our VTI forward solver. The equations for both cases are shown in the appendix A.

To compare the numerical wave propagation calculated with IFOS2D with the analytical one, we use a homogeneous model with the vertical P-wave velocity $v_{p,ver} = 500\,\frac{\mathrm{m}}{\mathrm{s}}$, the vertical S-wave velocity $v_{s,ver} = 300\,\frac{\mathrm{m}}{\mathrm{s}}$, the density $\rho = 1900\,\frac{\mathrm{kg}}{\mathrm{m}^3}$ and the Thomsen parameters $\varepsilon = 0.3$ and $\delta = 0.1$. The source is located at the center of the model to avoid numerical effects from the borders of the model. As source signal, a Ricker wavelet with a center frequency of 50 Hz is

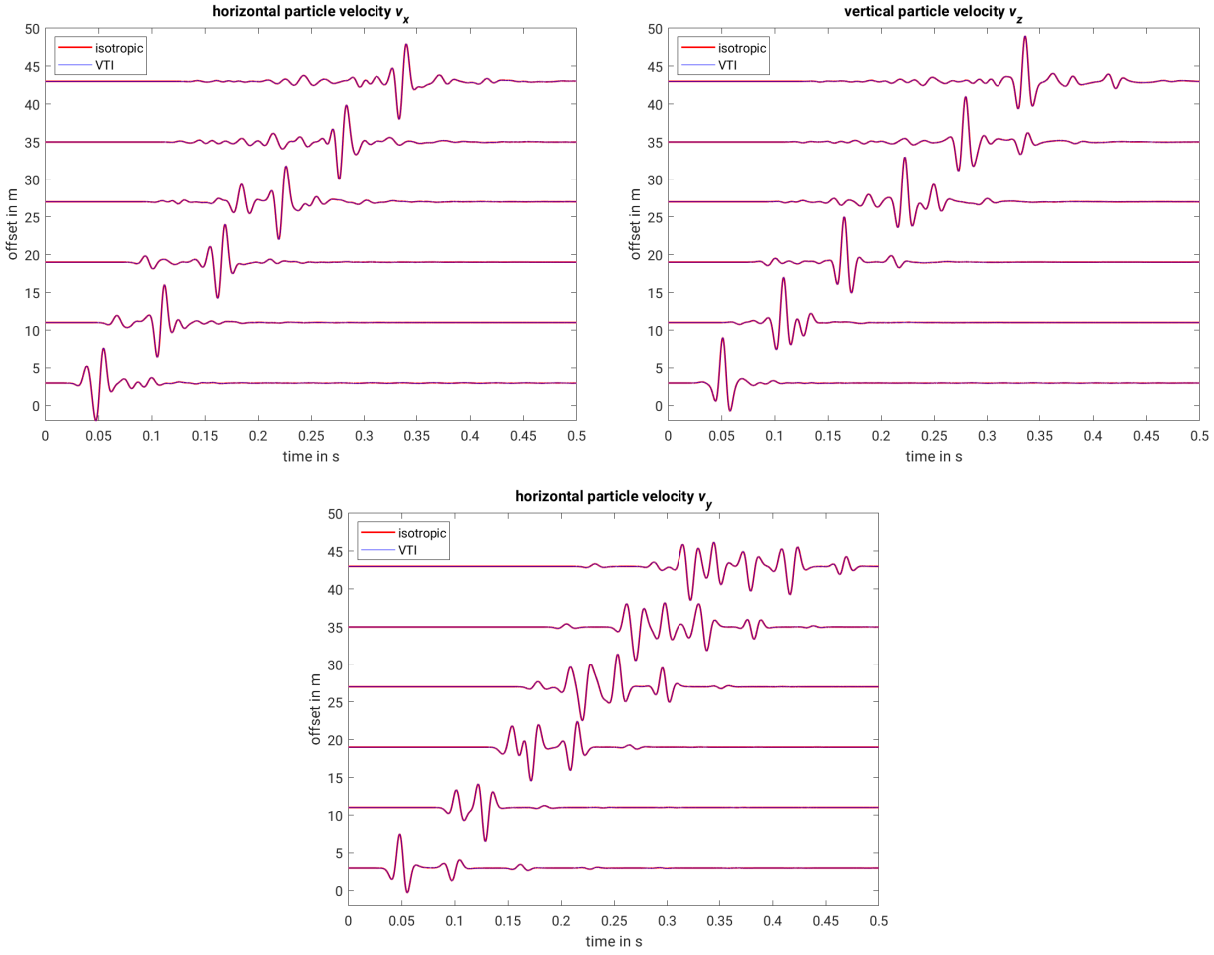

Figure 3.1.: Vertical (top left), horizontal inline (top right) and horizontal crossline component (bottom) of particle velocity calculated with the isotropic and the VTI forward solver.

used. Figure 3.2 shows snapshots of the numerical calculation at different timesteps overlayed by the analytically calculated position of the wavefronts. Since the Ricker wavelet is no zero phase wavelet and has instead its maximum at the time $t = 0$, the analytically calculated wavefronts do not correspond to the first onset of the wave but to its maximum. This corresponds exactly to what we see in figure 3.2: In all four snapshots, the analytically calculated wavefronts follow the second extremum of the numerical signal, which is the maximum of the Ricker wavelet. In the numerical solution at the first shown time step $t = 0.03\,\mathrm{s}$, the wavefronts of P and SV wave are near to each other and even overlapping at some points due to the short propagation time. For later times, they are clearly distinguishable and propagate according to the analytical solution. The comparison thus shows that the numerical solution reproduces the correct travel times in VTI media for both P- and SV-waves.

In a homogeneous isotropic medium, the waves would propagate with the same velocity in all directions creating circular wavefronts. In VTI media, the shape of the wavefronts changes due to the different velocities depending on the direction of propagation. As we can see in figure 2.3, the angle-dependency of P- and SV-wave velocities is different, which explains the different shapes of the wavefronts shown in the snapshots. For the P-wave, the horizontal velocity is about 30 % higher than the vertical velocity, which leads to an elliptical shape of the first wavefront. For the SV-wave, the horizontal and vertical velocities are the same, the fastest direction of propagation is in an angle of 45°. Therefore, the second wavefront is not elliptic but has an almost quadratic

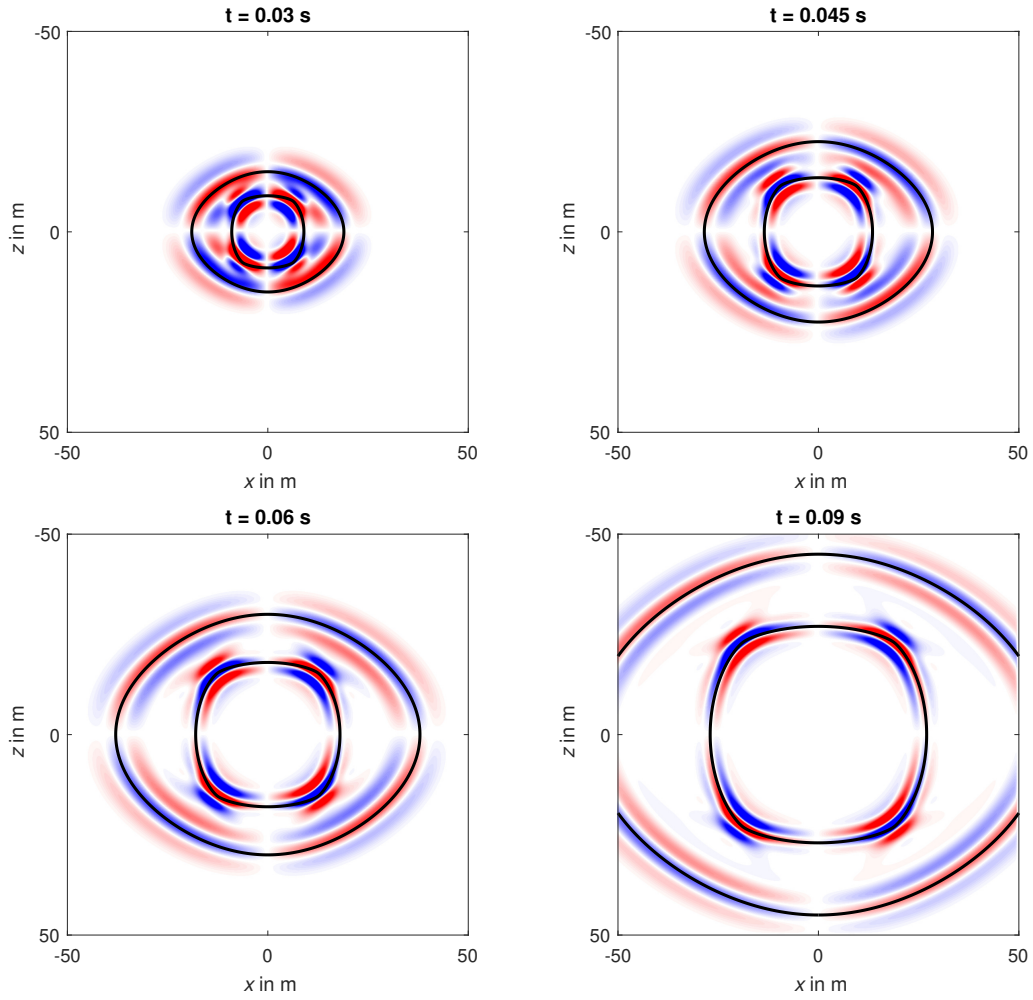

Figure 3.2.: Snapshots of wave propagation in VTI media calculated with IFOS2D compared to the analytically calculated wavefront (black line) after Payton (1983). The shown amplitudes represent the vertical particle velocities.

shape. The wavefront of the SH-wave (not shown here) would be similar to the P wavefront, with the shape of the ellipse defined by the third Thomsen parameter γ. The different behavior of SV- and SH-waves has an influence on the sensitivity of surface waves towards anisotropy, as we will show in detail in section 3.2.

The consistency of analytical and numerical wavefronts proves the correctness of the kinematic part of the numerical wave propagation, it ensures correct onsets and phase information. Since for FWI, not only the first onsets but the complete waveforms are used, we also have to ensure that the amplitudes are modeled correctly. To verify this, we compare the numerical solution at some single receivers to an analytical solution also provided by Payton (1983). This solution is only valid for sources and receivers located along the axis of symmetry, which is in our case the z-axis. Additionally, it is only possible to calculate the vertical displacement u_z for a vertically directed source and the horizontal displacement u_x for a horizontally directed source, since the other components are zero due to the radiation pattern of the sources. Figures 3.3 and 3.4 show the analytically and numerically calculated waveforms of horizontal and vertical displacement, respectively, with the source direction being vertical in the first figure and horizontal in the second one. We used the same model as for the calculation of the wavefronts with receivers located vertically below the source in offsets of 20 m and 40 m. The figures show an almost perfect

match of analytical and numerical solution. The accuracy of the fit depends on the discretization, so that the numerical solution becomes more and more accurate if time sampling Δt and grid spacing Δh are reduced. The shown seismograms were calculated with $\Delta h = 0.1\,\mathrm{m}$ and $\Delta t = 0.04\,\mathrm{ms}$.

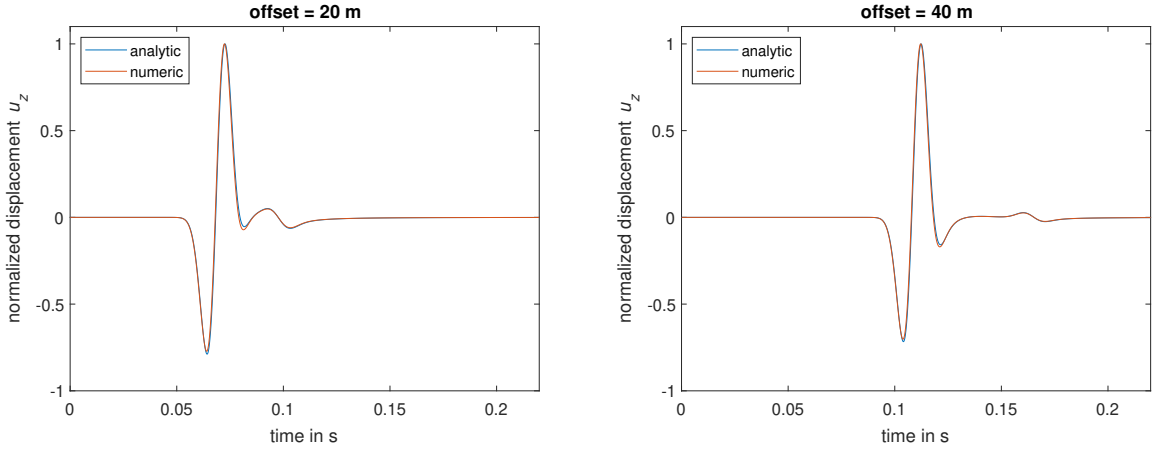

Figure 3.3.: Analytical and numerical solutions of the vertical displacement u_z evoked by a vertically orientated source at receivers located in offsets of 20 m and 40 m along the axis of symmetry (z-axis).

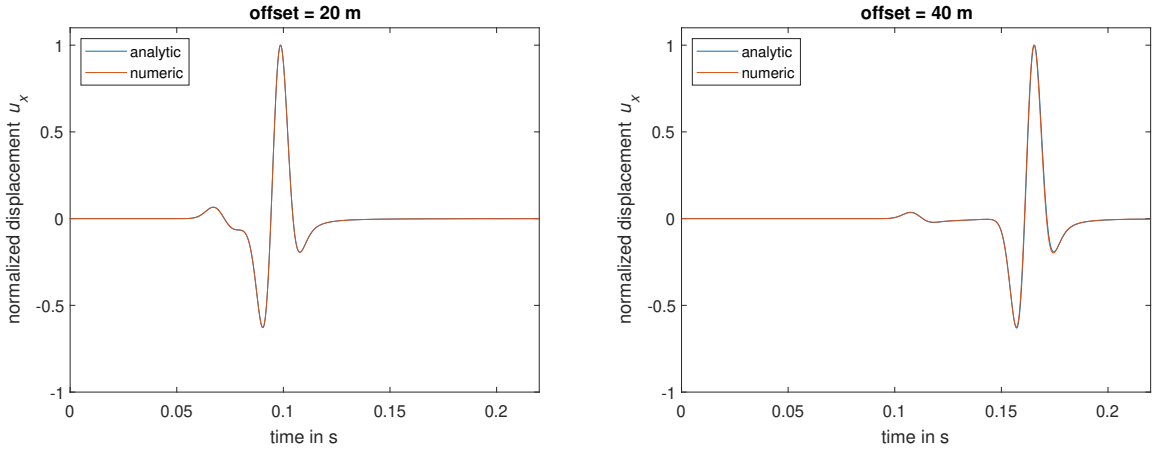

Figure 3.4.: Analytical and numerical solutions of the horizontal displacement u_x evoked by a horizontally orientated source at receivers located in offsets of 20 m and 40 m along the axis of symmetry (z-axis).

A correct forward calculation is essential for all following steps, e.g. for the sensitivity analysis and for FWI. The comparison of the VTI forward solver with the isotropic forward solver and the analytical solutions shows that the numerical calculation of wave propagation in VTI media gives the correct results, assuming that the discretization of the numerical grid is fine enough. Those observations guarantee that when working with field data, we will not introduce errors in FWI due to an incorrect forward modeling.

3.2. Sensitivity tests

If we inverted directly the data of all three velocity components, we would have to include three additional parameters to invert for. In addition to v_p, v_s and ρ, we would have to invert for the three Thomsen parameters, which gives us twice as much parameters than for the isotropic case. This does not only augment the computational costs significantly, but the increase of free

parameters also increases the number of possible models that can explain the observed data, which means that the inverse problem shows a higher ambiguity. To avoid or at least reduce those problems, we investigate first the effects of the Thomsen parameters on surface waves to see which parameter affects the most the waveforms and whether Love and Rayleigh waves show different sensitivities towards anisotropy. This sensitivity analysis can give us a clue about which parameters are the most important for the inversion and which ones could be neglected because of their lower influence on the waveforms.

3.2.1. Model setup

For the sensitivity test, we start with an isotropic, laterally homogeneous model and calculate the forward wave propagation in it. The model is derived from field data acquired at Bietigheim near Karlsruhe (Forbriger, 2003) and thus represents a realistic shallow subsurface model. It consists of a layered structure with velocities varying piecewise linearly with depth over a homogeneous halfspace starting at a depth of 16.4 m with $v_p = 1230\,\frac{\mathrm{m}}{\mathrm{s}}$ and $v_s = 715\,\frac{\mathrm{m}}{\mathrm{s}}$. The density model consists of only two layers with a value of $2300\,\frac{\mathrm{kg}}{\mathrm{m}^3}$ in the halfspace and $1600\,\frac{\mathrm{kg}}{\mathrm{m}^3}$ above. The vertical profiles of velocities and density are shown in figure 3.5. For the numerical calculation, the model consists of 800 x 300 grid points with a spacing of 0.1 m, which corresponds to a model size of 80 m in x- and 30 m in z-direction. The total recording time is 0.6 s with a time sampling of 0.04 ms. A source is located at $x = 5$ m which emits a Ricker wavelet with a center frequency of 50 Hz and the receivers are located at the surface every 3 m. The source is directed vertically for the emission of P- and SV-waves and horizontally for SH-waves.

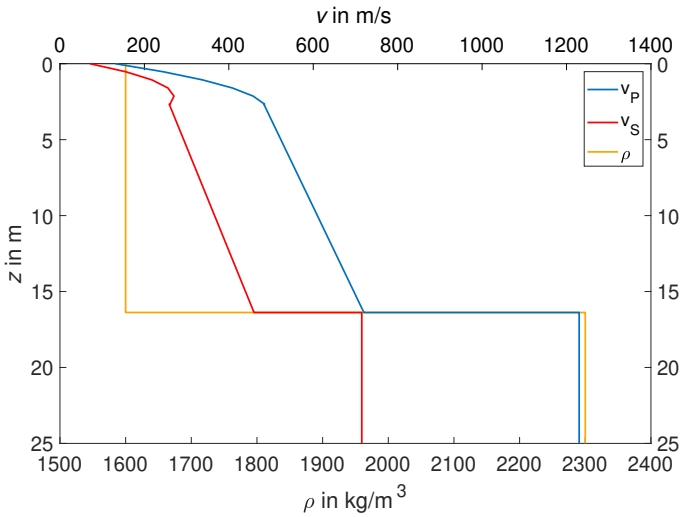

Figure 3.5.: Vertical profiles of P-wave velocity v_p, S-wave velocity v_s and density ρ in the laterally homogeneous model used for the sensitivity analysis.

In a next step, we introduce anisotropy into our model. We therefore use the velocities from the isotropic model shown in figure 3.5 as vertical velocities in a VTI model and define the horizontal velocities through the Thomsen parameters. By variation of the parameters ε, δ and γ from 0 to 0.1, we get various VTI models with different grades of anisotropy. The maximal values of 0.1 correspond approximately to a difference of horizontal and vertical velocity of 10 %, which is a common value for sedimentary rocks. For each model, only one of the Thomsen parameters is varied while the other two are kept to zero. This method allows us to investigate the direct effect of all three parameters separately without considering the interference of ε and δ in the velocities of P- and SV-waves (see equations (2.1) - (2.3)). For each VTI model, we calculate the wave propagation so that we can compare the waveforms recorded at the receivers to the isotropic case.

3.2.2. Sensitivity of Rayleigh waves

Figure 3.6 shows the seismograms of particle velocities at an offset of 30 m for the x- and z-component, where the main part of the signal is formed by the Rayleigh wave. On those two components, the parameter γ has no effect, since no SH-waves are recorded. We therefore compare the seismograms calculated in the VTI models with the values $\varepsilon = 0.1$ and $\delta = 0.1$ to those calculated in the isotropic model. The seismograms show that both parameters induce a change of the waveforms concerning both travel times and amplitudes. The effects on both components are similar since both contain parts of P-, SV- and Rayleigh waves. In the model with $\varepsilon = 0.1$, the complete duration of the recorded signal becomes shorter than in an isotropic model, and the first onset of the P-wave appears earlier. Those differences are explained by the higher horizontal velocity of P-waves which leads to a faster propagation of the direct P-wave and the Rayleigh wave in the VTI medium.

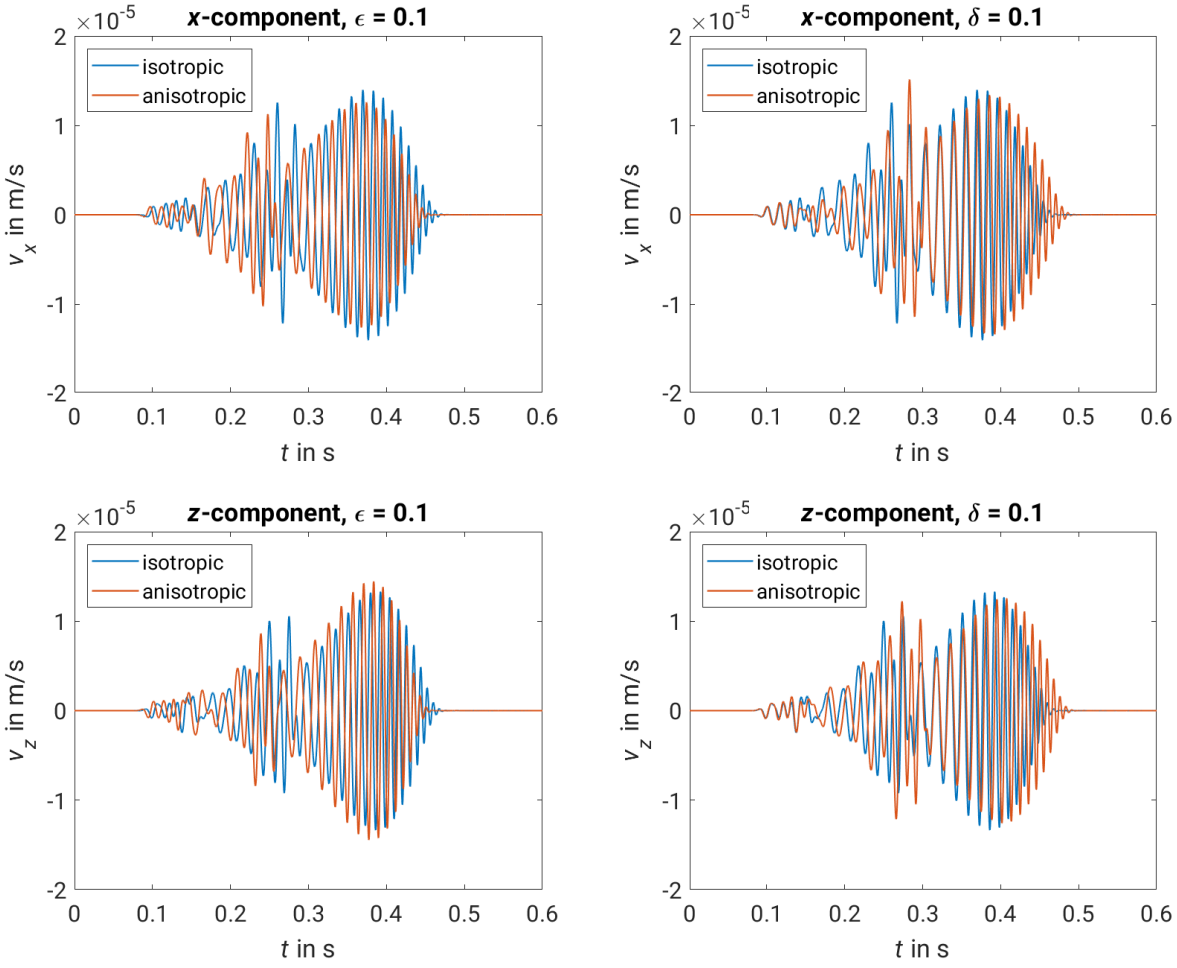

Figure 3.6.: Particle velocity seismograms at the same receiver in an offset of 30 m for the z-component (top row) and the x-component (bottom row). Each subplot shows the result in an isotropic model (blue) compared with the result of a VTI model (red). For the left-hand side, a model with $\varepsilon = 0.1$ and $\delta = 0$ was used, for the right-hand side a model with $\varepsilon = 0$ and $\delta = 0.1$.

For the model with $\varepsilon = 0$ and $\delta = 0.1$, the observable effects are different. The first onset of the direct P-wave is equal to the isotropic waveform, but later arrivals are later in time in the VTI model. The VTI and isotropic waveforms are again almost equal at the beginning of the

Rayleigh wave, but for later times the VTI waveform gets retarded so that the total duration of the signal is longer than in the isotropic case. If we take a look at the angle-dependency of the wave velocities, we see that for the chosen Thomsen parameters, the horizontal P- and SV-wave velocities are equal to the vertical velocities and thus to the isotropic ones. This explains the similarity of the direct waves and of parts of the Rayleigh wave, since purely horizontally propagating waves are not affected by the parameter δ. However, the Rayleigh wave seems also to be affected by the non-horizontal velocities, which influence the ellipticity of Rayleigh waves. Differing from the model with $\varepsilon = 0$, the waves are propagating slower in a VTI medium because of the negative sign before δ in equation (2.2), which reduces the velocities for propagation in directions different from the horizontal or vertical one.

An interesting conclusion of those observations is that even if the wavefield consists mainly of horizontally propagating waves as direct and surface waves and the horizontal velocities are equal to the isotropic ones, the wavefield is still affected significantly by anisotropy. The sensitivity towards ε and δ is in a similar range of magnitude, but has different, partially opposite effects on the waveforms. If we have more complex models where none of both parameters are zero, it will become difficult to separate the influences of both parameters since it could happen that the effects of one parameter are compensated by those of the other one.

3.2.3. Sensitivity of Love waves

A similar study is now done for the SH-component of the wavefield. For this component, only the parameter γ is relevant, so we use the S-wave velocities shown in figure 3.5 as vertical velocities $v_{s,ver}$ and create models with different horizontal velocities $v_{s,hor}$ by varying γ up to 0.1. Additionally, we create a second set of VTI models where we use the isotropic velocity as horizontal velocity and vary the vertical velocity via the parameter γ. This allows us to investigate differences in the sensitivities towards horizontal and vertical velocity, since we keep in the two cases one of both velocities constant.

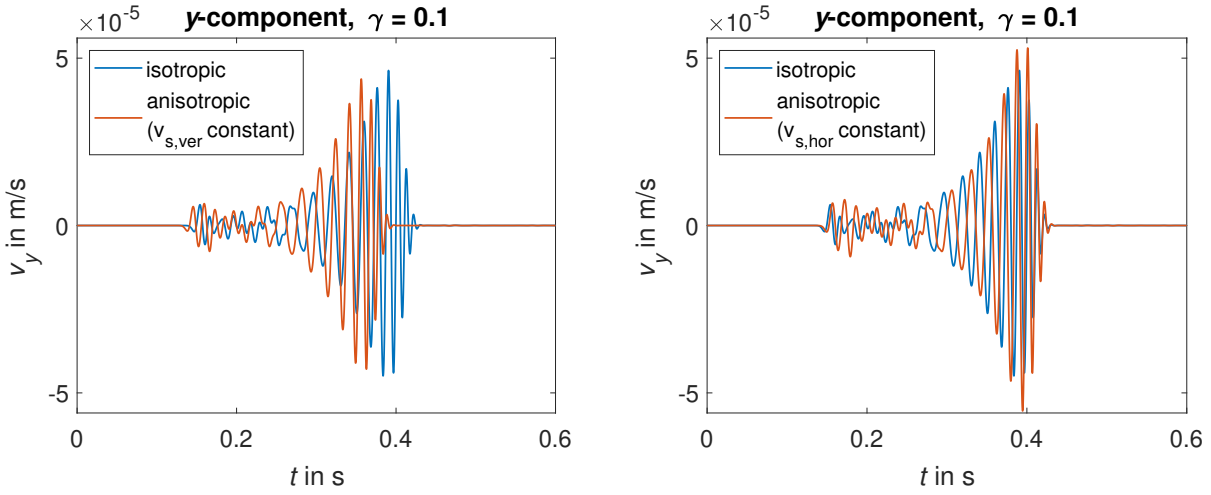

Figure 3.7.: Particle velocity seismograms at the same receiver in an offset of 30 m for the y-component. Each subplot shows the result in an isotropic model (blue) compared with the result of a VTI model with $\gamma = 0.1$ (red). On the left-hand side, the vertical velocity $v_{s,ver}$ and on the right-hand side the horizontal velocity $v_{s,hor}$ is equal to the isotropic v_s.

Figure 3.7 shows the results for the two models with $\gamma = 0.1$. In both models, the horizontal velocity is higher than the vertical one, their difference is that the isotropic velocity corresponds to the vertical or the horizontal velocity, respectively. The use of those two models allows us to

study the sensitivity towards horizontal and vertical velocity separately, since in the two models only one of both velocities is varied. In the model where the vertical velocity is kept constant (equal to isotropic velocity), the waves are propagating significantly faster than in the isotropic model. From the first onset on, the phases are shifted to earlier times, for the Love wave, the time difference between corresponding phases amounts up to three times the period, which means that multiple cycle-skipping occurs. This effect is not surprising, since the direct SH-wave and Love wave are propagating horizontally with a velocity that is about 10 % higher than in the isotropic model. Apart from the phase shifts, the differences between the seismograms are rather small, only slight changes in amplitudes and waveforms can be observed.

A completely different result is obtained for the model with constant horizontal velocity. Here, the total duration of the signal does not change at all, the isotropic and VTI signals are starting and ending at the same time. However, in between, there are high differences between the seismograms concerning the waveform and also the amplitudes. Those changes of the waveform also induce a time difference between corresponding phases of up to one period, which is less than for the first model, but high enough that cycle skipping occurs so that in FWI wrong phases would eventually be fitted.

All in all, the tests showed that the Love wave is sensitive towards both horizontal and vertical velocities. A differing horizontal velocity leads mainly to kinematic changes, while the vertical velocity has stronger dynamic effects and induces changes of waveform and amplitudes. Equivalent to the Rayleigh wave, the Love wave is also affected by the vertical velocity, even if it is propagating horizontally. This sensitivity towards both parameters is a basic requirement for successful FWI, beacause if one parameter would have only very small effects on the waveforms, it would be impossible to reconstruct it with FWI.

3.2.4. Comparison and conclusions

On a first look at figures 3.6 and 3.7, we can already see that the SH-component is stronger affected by anisotropy than the two other components. To be able to compare the effects quantitatively, we calculate for different VTI models the L2 norm by summing up the squared differences of isotropic and VTI particle velocities from 24 receivers placed in 3 m-intervals. For the models, we vary the parameters ϵ, δ and γ respectively from 0.01 to 0.1 in steps of 0.01, so that we get 10 models for each Thomsen parameter. For the SH-component, we again differ between models with $v_{s,ver} = v_{s,iso}$ and $v_{s,hor} = v_{s,iso}$.

Figure 3.8 shows the resulting L2 values for all components and models. For the Rayleigh wave, the plot matches our observations in the seismograms: The L2-curves of x- and z-component show only very small differences, and also the effects of ε and δ are in a similar range of magnitude, the models with non-zero ε values generate only slightly higher L2 values. However, the L2 norm of the SH-component is significantly higher (up to four times) for all grades of anisotropy, and this regardless whether the horizontal or the vertical velocity is changed. An interesting fact is that the curves for the two SH cases are intersecting at $\gamma = 0.04$. This means that if we use the L2 norm as a measure for the sensitivity, then at least for this model, the Love waves are for weak anisotropy more sensitive to the horizontal velocity, and for higher values of γ more sensitive to the vertical velocity. This does not seem to be very intuitive, as Love waves propagate horizontally, we would expect a higher sensitivity towards the horizontal velocity over the whole range of γ. On the other hand, the seismograms in figure 3.7 already showed that the vertical velocity also influences the waveforms, but in a different way than the horizontal velocity. The similarity of the L2 norm in both models might be caused by cycle-skipping. A signal that is shifted by one complete period relative to the isotropic signal may have a smaller misfit than a less shifted signal,

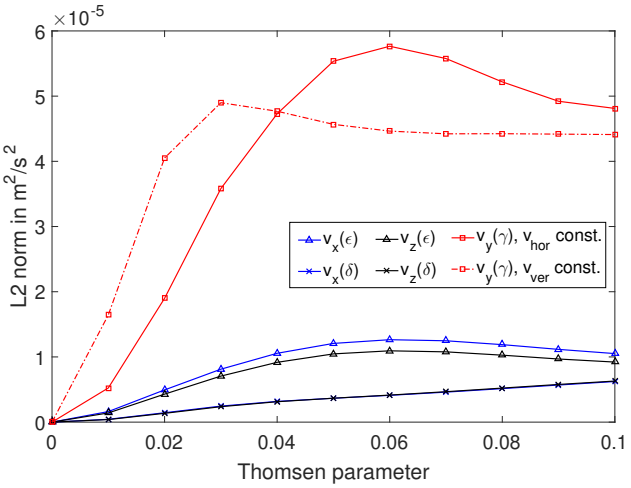

Figure 3.8.: L2 norm of particle velocities for all three components. The values for the x- and z-components were calculated for models with varying ε and δ, the y-component for models with varying γ. For all curves, 24 receivers with spacings of 3 m were used.

because with a phase shift of 2π, the phases are overlaying again, although different phases are then compared. Due to the cycle-skipping, it is possible that the sensitivity towards the vertical velocity is higher when measured by the L2 norm. Cycle-skipping explains also why the misfit is not increasing continuously with γ. The maximal misfit is reached for a value of γ where the signal is shifted by about half a period. For higher γ, the misfit does not increase further or even gets smaller, since the phase information becomes then again more similar to the isotropic signal.

If we used a different norm, as for example an envelope-based norm, this would be completely different. As we can see in figure 3.7, the envelope of the signal is almost not affected by a change of the vertical velocity, so that the misfit would be very small in this case. On the other hand, for the model with differing horizontal velocity, the envelope of the signal is clearly changed, so that we would have a stronger sensitivity towards the horizontal velocity when using such a norm. In this case, the misfit would also increase continuously with γ, since the effects on the envelope are mainly based on the time shifts of the signal, which increase gradually with γ.

In summary, the sensitivity tests showed that both Love and Rayleigh waves are affected by anisotropy, but with Love waves showing a much higher sensitivity. It is valid for all components that not only the horizontal velocity affects the waveforms of the surface waves, but also the vertical one, even if the direction of propagation is mainly horizontal. The horizontal velocity has mostly kinematic effects leading to time shifts of the signal, while the vertical velocity has a higher influence on the waveform and on amplitudes. Because of the significantly higher sensitivity of Love waves, we will focus in this work on the inversion of SH data. The SH case has the additional advantage that only one additional parameter compared to the isotropic case, the Thomsen parameter γ, is needed, which reduces the complexity of the problem and the computational costs. We showed in this section that when using the L2 norm as misfit function, a sensitivity of Love waves towards horizontal and vertical velocities is given, while a different norm would probably enhance the sensitivity towards the horizontal velocity but reduce it towards the vertical velocity. We will therefore use for FWI the L2 norm as objective function, since it allows us at least theoretically to reconstruct both parameters. The results of the sensitivity analysis give us good preconditions for a successful FWI of SH data. A sensitivity towards all parameters is given, and due to the different effects of the parameters, the ambiguity of the inverse problem will be kept limited even with an additional parameter. The possibilities and limitations of the

anisotropic FWI will be shown in the following sections by its application on synthetic and real data.

4. Inversion of synthetic data

In this chapter, we show a few tests of the anisotropic FWI calculated with synthetic data. The data is created by calculating the anisotropic wave propagation numerically in a given model. We use for the tests different models, starting with a laterally homogeneous model and augmenting the complexity by introducing lateral variations. An additional test is carried out to investigate the effects of crosstalk between different model parameters.

4.1. Layered model

4.1.1. Models and inversion settings

As a first synthetic model for testing the inversion, we use a model consisting of two layers over a halfspace with all layers having a VTI structure. Both layers have a thickness of 3 m and the velocities and densities are shown in table 4.1. The relative velocity difference between fast and low direction is in all layers about 10 %, but only in the second layer the vertical velocity is higher than the horizontal one, which corresponds to a negative value of γ. The whole model has a length of 51 m and a depth of 15 m and is discretized with a numerical grid with equal spacings of $\Delta h = 0.1$ m, which creates a grid of 510 x 150 = 76500 grid points.

Table 4.1.: Velocities and densities of the layered model used for a synthetic FWI test. The parameter z indicates the depth of the top edge of the layers.

Layer	z in m	$v_{s,ver}$ in m/s	$v_{s,hor}$ in m/s	ρ in $\frac{\text{kg}}{\text{m}^3}$
1	0	180	200	1900
2	3	250	230	2000
Halfspace	6	330	300	2100

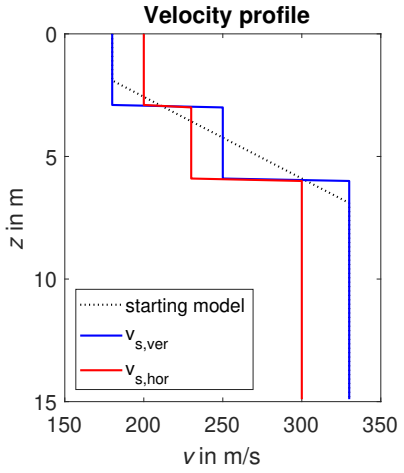

Figure 4.1.: Vertical profile of true and initial models of horizontal and vertical velocities.

As initial velocity model for the inversion, we use an isotropic model based on the vertical velocity. For the first 2 m and from depths of 7 m on, the true vertical velocities are used, in between they are connected by a linear gradient. For the density, we also use a linear gradient from 1900 $\frac{\text{kg}}{\text{m}^3}$ to 2100 $\frac{\text{kg}}{\text{m}^3}$ between 2 m and 7 m depth. In figure 4.1, a vertical profile of true and initial models is shown. We avoid to include hard interfaces in the initial models, since they will hardly be changed during the inversion.

The acquisition geometry in this synthetic test consists of 48 receivers located at the surface every 1 m from $x = 3$ m on, and of 10 sources every 5 m with the first source being located at

$x = 2\,\mathrm{m}$. The sources are horizontally directed and emit a Ricker wavelet with a center frequency of 50 Hz. During the inversion, we will not invert for the source time function but use the same source wavelet as for the forward calculation. For the model described in table 4.1, we perform an elastic VTI forward calculation to produce the pseudo-observed data that will be used for the inversion. The total recording time is set to 0.4 s and a time sampling of 0.04 ms is used to guarantee numerical stability. In this test, no noise is added to the data.

As objective function $J(m)$ of FWI, we use the L2 norm

$$J(m) = \frac{1}{2} \int \sum_{r,s} ||v_{syn} - v_{obs}||^2 \, dt \tag{4.1}$$

because of its sensitivity towards horizontal and vertical velocities (see section 3.2). Here, v_{obs} are the pseudo-observed particle velocities, v_{syn} the particle velocities calculated in the actual model during the inversion and the sum over r and s denotes the summation over all sources and receivers. For the synthetic case, no normalization of the traces in the seismograms is necessary. The pseudo-observed data and the forward modeling during the inversion are calculated with the same forward solver, so that all amplitude information of the data can be explained when the true model is reached by the inversion. In each iteration, the model updates for $v_{s,ver}$, $v_{s,hor}$ and ρ are calculated simultaneously as described in section 2.3 by using the PCG method (Polak and Ribière, 1969). To reduce cycle skipping and thus avoid local minima of the objective function, we apply the FWI in different stages with increasing frequency content (Bunks et al., 1995). In the first inversion stage, we apply a low-pass filter with a corner frequency of 5 Hz on the data, and in each stage this corner frequency is increased by 10 Hz until all frequencies up to 95 Hz are used. Each stage has the same abort criterion, the next stage starts either if no step length is found that reduces the misfit or if the relative reduction of misfit compared to the second last iteration is less than 1 %. To avoid strong small-scale fluctuations of the model parameters, the gradients are smoothed in each iteration with a 2D median filter with a filter length of 5 grid points. Additionally, we apply circular tapers around the sources with a radius of 0.5 m to avoid strong model updates at the source locations.

4.1.2. Results

The inversion finished after 394 iterations and managed to reduce the misfit from $1 \cdot 10^{-1}\,\mathrm{m^2/s^2}$ in the first iteration to only $3.6 \cdot 10^{-5}\,\mathrm{m^2/s^2}$ as final value. The misfit curve is shown in figure 4.3. The misfit is not decreasing continuously, but is jumping to higher values each time the inversion changes to the next stage with a higher frequency content. Due to the different data used in each stage, the misfit values of different stages are not directly comparable. However, we can see that in each stage the misfit is decreasing continuously, so that for each frequency interval the inversion managed to improve the data fit. We also see that the main part of misfit reduction happens in the first stage, i.e. for the data filtered with 5 Hz. In this stage, we have with 86 iterations the highest number of iterations of all stages and the strongest changes of misfit. This means that the model is mainly defined in this stage, and for higher frequencies, where smaller wavelengths are included, only small-scale details of the model are changed. In the simple model used for this test, we have no small-scale features that could only be resolved with higher frequencies.

The final models are shown in figure 4.2 together with the true models. The inverted $v_{s,ver}$ model shows an almost perfect result, the three layers are sharply separated from each other and the absolute velocities of all layers have the correct values. Especially in the deeper part, we see the effects of the acquisition geometry that allows a good reconstruction of the subsurface in the

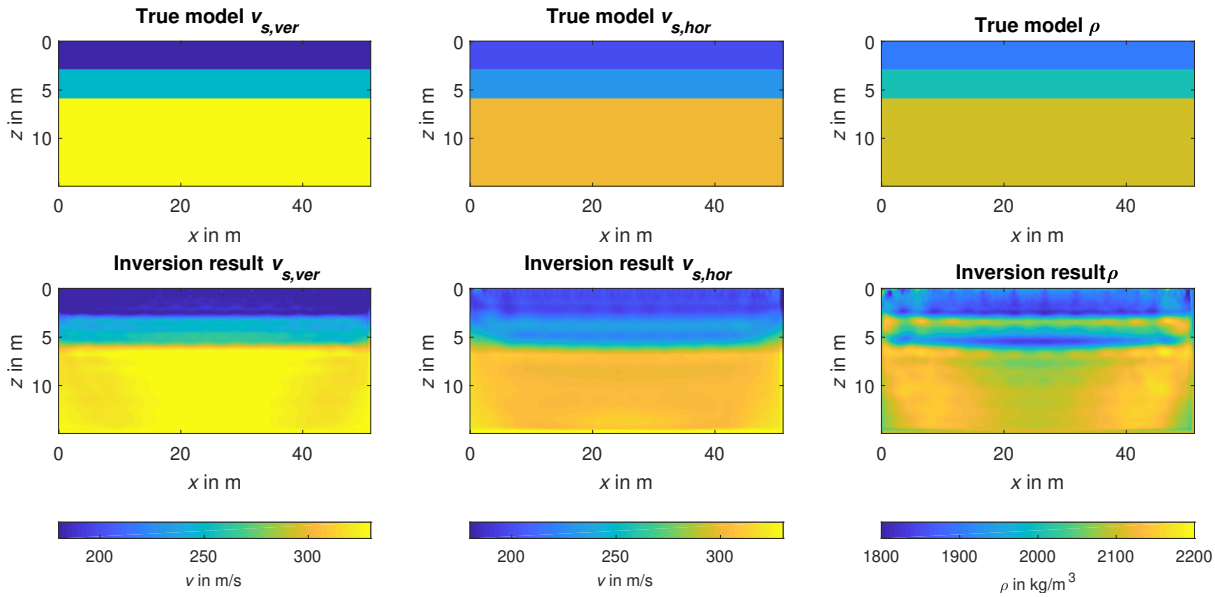

Figure 4.2.: True models and results of the VTI inversion after 394 iterations for vertical velocity $v_{s,ver}$, horizontal velocity $v_{s,hor}$ and density ρ.

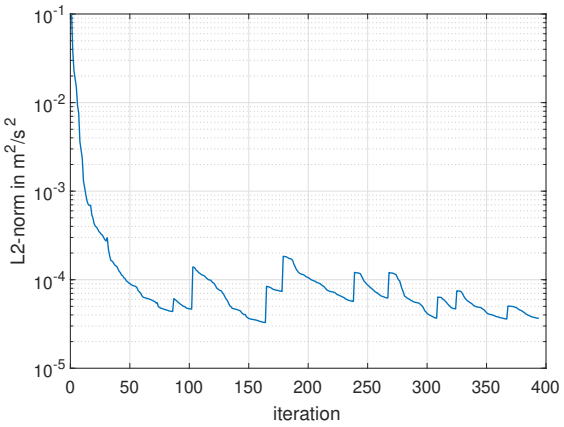

Figure 4.3.: L2 misfit plotted over the number of iteration. The jumps in the misfit function correspond to increases of the frequency content of the data used for the inversion.

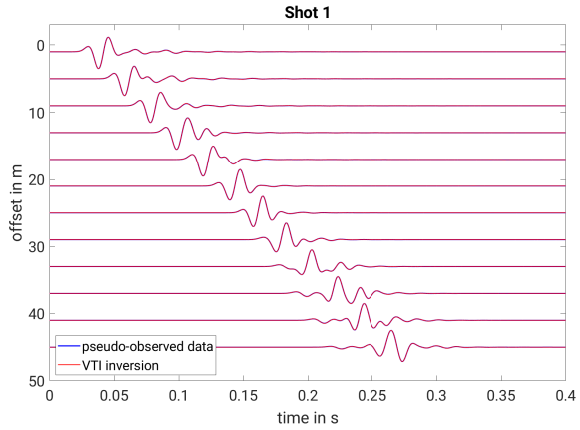

Figure 4.4.: Pseudo-observed data (blue) and velocity seismograms calulated in the final inverted models shown in figure 4.2 (red) for the first shot located at $x = 2\,\mathrm{m}$.

central part of the model and gives worse results at the sides that can only be seen, if any, by a few rays. The inversion gives also a very good result for $v_{s,hor}$, here, the interfaces are not resolved as sharp as for the vertical velocity, but still the three layers are distinguishable. Unlike the vertical velocity, the horizontal velocities at shallow depths and for depths greater than 7 m had not already the true values in the initial model. However, the velocities of all layers were reconstructed correctly. Even for great depths up to the lower boundary of the model, where only a small part of the wavefield is traveling, the values of $v_{s,hor}$ correspond to the true values. Worse results are obtained for the inverted density model. Here, the first two layers are resolved with approximately the correct values, but at the interfaces strong oscillations appear that could be wrongly interpreted as thin density anomalies. The differences in quality between the v_s-models and the density are not surprising, since it is well-known that surface waves are mainly affected by the S-wave velocities in the subsurface and show only a weak sensitivity towards ρ. Therefore, the data fit is mainly optimized by changes of the v_s-models, while changes in the density model

have only small effects on the misfit. Thus, the resulting density models are not really reliable, but on the other hand errors of this parameter have no significant effects on the results of the two velocity parameters.

Because of the convergence of the misfit and the good reconstruction of the velocity models, it is obvious that also the seismograms obtained from the final model should be similar to the pseudo-observed seismograms calculated in the true model. This can be seen in figure 4.4, where the seismograms of a few receivers are compared for the first shot (located at $x = 2\,\mathrm{m}$). The seismograms are not distinguishable, so that the models resulting from the inversion give an accurate explanation of the observed data.

We showed with this example that the anisotropic FWI is working almost perfectly on a simple synthetic, noise-free model. In the following sections, we will increase the complexity of the model by adding lateral variations and anomalies to investigate further capabilities of the inversion.

4.2. 2D model

4.2.1. Models and inversion settings

For our next synthetic test, we use a more complex model with lateral variations of the velocities and with different structures of horizontal and vertical velocity. For $v_{s,hor}$, we use as before a model consisting of two layers of 3 m thickness over a halfspace. In the vertical velocity model, we add a vertical interface in the middle of the model, so that the model is split into six different blocks with different velocities. For the density, we keep the layered model from the previous test. All velocities and densities of the models can be found in table 4.2 and the models are also shown in figure 4.5 a). Model size, acquisition geometry and numerical discretization are the same than in the previous example.

Table 4.2.: Velocities and densities of the model with lateral variations of $v_{s,ver}$ used for a synthetic test of FWI.

Layer	z in m	$v_{s,ver}$ in m/s (left side)	$v_{s,ver}$ in m/s (right side)	$v_{s,hor}$ in m/s	ρ in $\frac{\mathrm{kg}}{\mathrm{m}^3}$
1	0	180	190	200	1900
2	3	250	220	230	2000
Halfspace	6	330	280	300	2100

As initial models, we use for both velocities the same linear gradient model which is based on the true $v_{s,hor}$ model. For ρ, a linear gradient model is also used. The initial models can be seen in figure 4.5 b). All inversion parameters are identical to the previous synthetic example of the layered model. In addition to the VTI inversion of the pseudo-observed data, we also apply an isotropic FWI to the same data. In this case, the inversion tries to explain the effects of anisotropy in the data by an isotropic model, and by comparing the results of the two inversions it can be seen which effects it has on FWI to ignore anisotropy.

4.2.2. Results

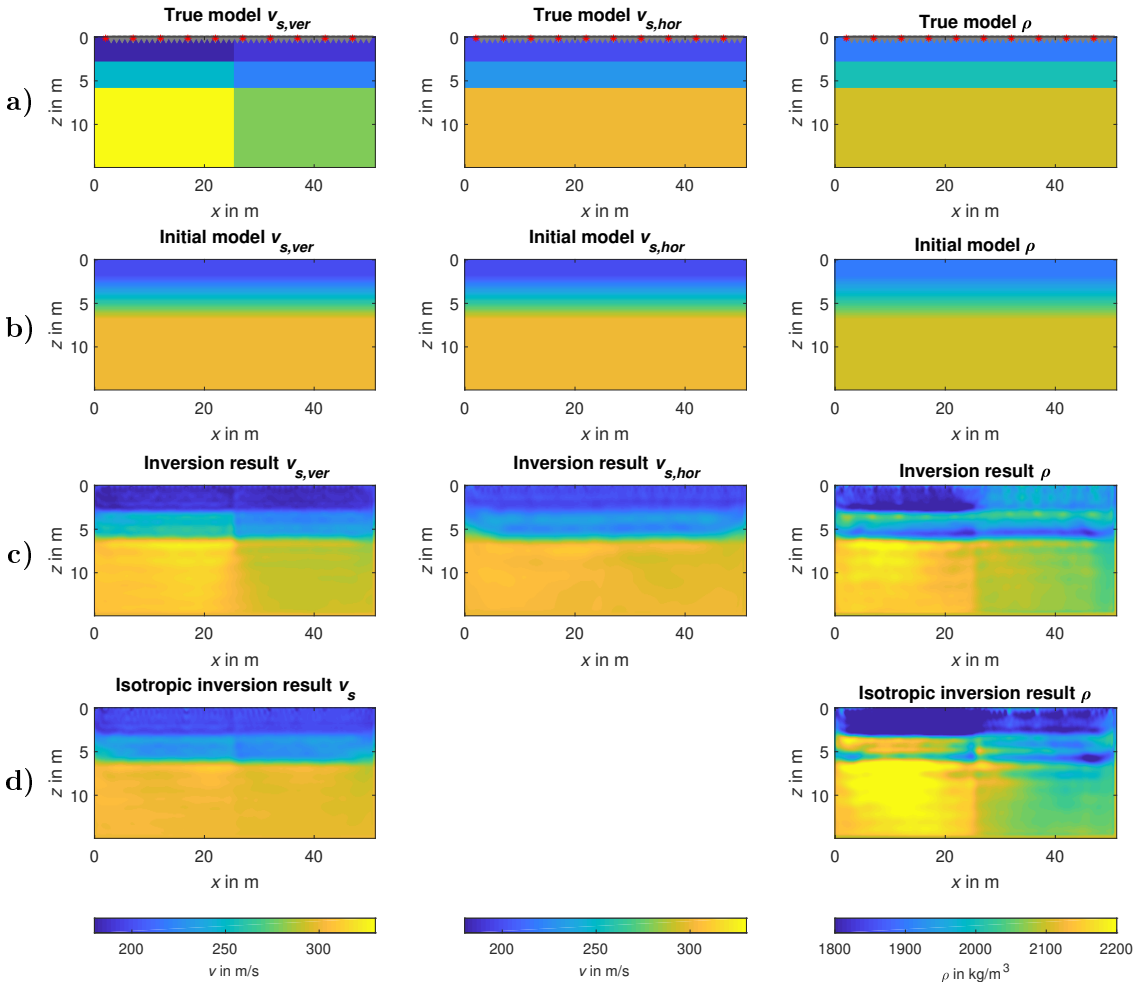

Figure 4.5.: **a)** True models used to produce the pseudo-observed data. **b)** Initial models for the inversion. **c)** Results of the anisotropic FWI. **d)** Results of isotropic FWI applied on the VTI data.

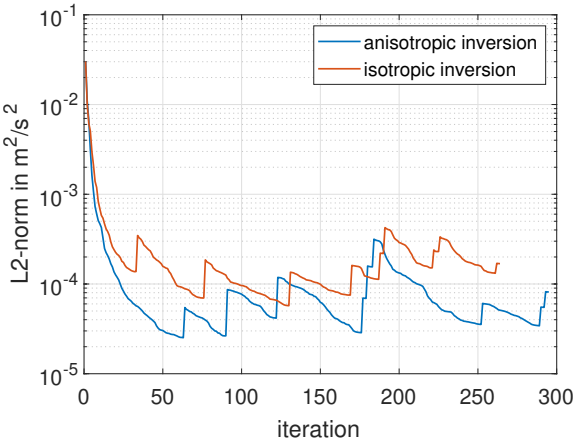

Figure 4.6.: L2 misfit of VTI and isotropic FWI plotted over the number of iteration. The jumps in the misfit function correspond to increases of the frequency content of the data used for the inversion.

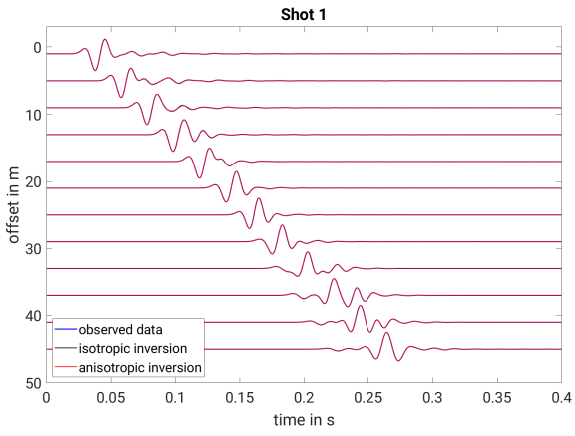

Figure 4.7.: Pseudo-observed data (blue) and velocity seismograms calculated in the final inverted models of anisotropic (red) and isotropic FWI (black) for the first shot located at $x = 2\,\mathrm{m}$.

In figures 4.5 c) and d), the results of anisotropic and isotropic FWI are shown, respectively. With the anisotropic inversion, good results for horizontal and vertical velocities are obtained. For $v_{s,ver}$, all interfaces are clearly visible in the inversion result, so even the lateral velocity structure could be reconstructed although the initial model was laterally homogeneous. In the first two layers, the inverted velocities match almost perfectly the true velocities, but in the halfspace, the model updates were not strong enough relatively to the initial model, so that the final model shows too low velocities in the left part and too high velocities in the right part with differences to the true velocities of about $10\,\frac{\mathrm{m}}{\mathrm{s}}$. The inversion result for the horizontal velocity is very similar to the result of the inversion for the purely layered model without lateral variations (see figure 4.2). This shows us that the lateral variations in $v_{s,ver}$ seem to have no effect at all on the inversion of horizontal velocity, which is a good sign since it shows that the effects of both parameters on the waveforms can be separated by the inversion. As in the results of the layered model, the interfaces in $v_{s,hor}$ are not reconstructed as sharply as for $v_{s,ver}$, but are still clearly visible. The inverted density shows a rather poor result, here the true structure of three laterally homogeneous layers is not resolved properly, instead the density model shows the same structure as $v_{s,ver}$ with different values in the left and the right part of the model. We thus see here a strong crosstalk between ρ and $v_{s,ver}$, which we will investigate further in section 4.3.

When using an isotropic inversion, we get as a result in addition to the density model only one velocity model, which should explain the data created in a model with different horizontal and vertical velocities as good as possible. The inversion result of v_s for this example (figure 4.5 d) is somewhere inbetween the true horizontal and vertical velocities. Especially in the shallow part of the model, the structure of $v_{s,ver}$ is clearly visible, the halfspace however looks almost laterally homogeneous and has a similar value as the true horizontal velocity of this part. The density model looks similar to the result of the anisotropic inversion, but the crosstalk with the vertical velocity is even stronger and there are more artifacts in the shallow part of the model. Since we have only one velocity model to explain both different true models, all other effects of anisotropy on the waveforms that can not be explained by v_s are projected into the density model, so that the retrieved density itself becomes useless, but helps to improve the result of inverted velocity. This effect can easily be shown by inverting only for the velocities while the density is not inverted but the true density model used during the whole inversion. That case is shown in figure 4.8 for VTI and isotropic FWI. For the anisotropic FWI, the ambiguity of the inverse problem is reduced if the true density model is given and kept constant. Therefore, the results for both velocity models are improved and show an almost perfect reconstruction of the true models. The improvements can especially be seen in the vertical velocity, where now even for the deeper parts of the models the true velocities are resolved. When we included the density into the inversion process, some features of the velocity models were thus projected into the density model which leads to slightly worse results for the velocities. In the case of the isotropic FWI, the effects are opposite to this. Here, the inversion of only v_s has the effect that all anisotropic effects have to be explained by one single model. The resulting model is more similar to the true horizontal velocity, but shows also lateral differences caused by the true vertical velocity model. Compared to the isotropic inversion with non-constant density model, the velocity model now contains strong artifacts, especially in the left part of the model. When inverting also for density, those artifacts can be avoided by changes in the density model which yields a falsified density model but gives a realistic velocity model.

When working with field data, normally the density is also inverted in addition to the velocities, since the true density model is not known. As we showed in this example, the isotropic result for v_s looks in this case quite realistic and contains no artifacts that could be an indication for anisotropy. The comparison of misfit values and the data fit (figures 4.6 and 4.7) shows also

no significant differences between isotropic and VTI inversion. This makes it problematic to recognize an anisotropic subsurface directly from the inversion result. It is possible to get an isotropic inversion result that explains the anisotropic data almost as good as a VTI model. It is not evident from the resulting model, the data fit or the misfit curve that the observed data corresponds to an anisotropic model. Because of the higher computational time of VTI FWI, it does not make sense to use directly an anisotropic inversion on every data set. Therefore, it is essential to know before inverting the data if the subsurface could possibly have a VTI structure. In this case, it would be useful to use the VTI FWI to obtain a more correct and more detailed model of the subsurface.

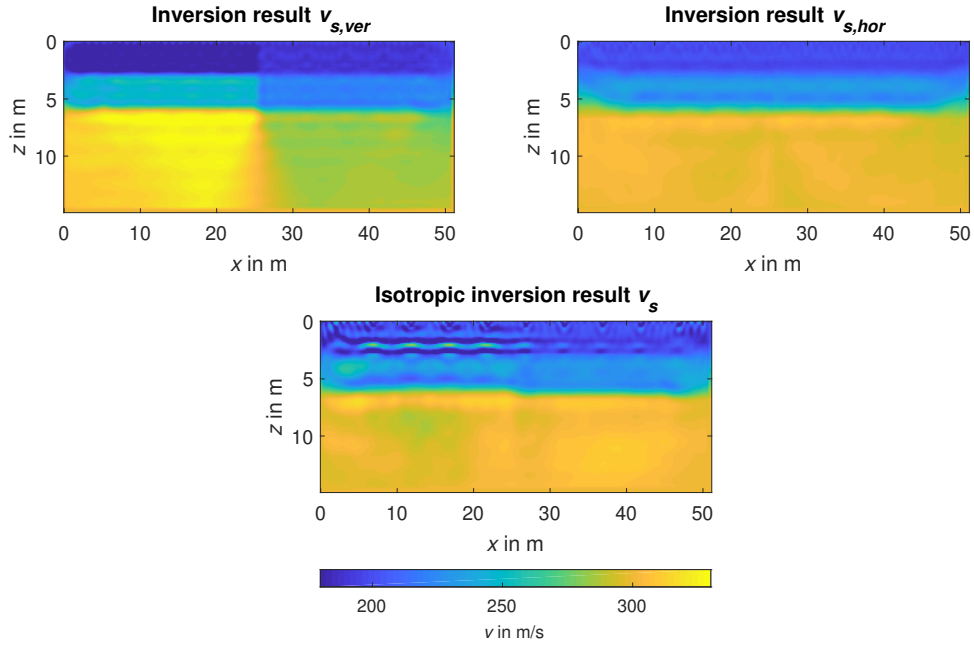

Figure 4.8.: Resulting velocity models of VTI and isotropic FWI when the density is kept constant to the true density.

For the sake of completeness, we perform the same synthetic test with switched true models of horizontal and vertical velocity, so that we now have lateral velocity variations in $v_{s,hor}$. All other inversion parameters are kept the same than for the previous test. This additional test should show if for example lateral variations can be better resolved for one of the velocity parameters or if the differences between VTI and isotropic inversion are stronger for one of both cases. The true and initial models as well as the results of isotropic and VTI inversion are shown in figure B.1 in the appendix. The quality of the results of the anisotropic inversion is similar to the example with swapped velocity models (see figure 4.5), the different spatial structures of both velocity models are reconstructed correctly, and also the velocity values correspond well to those of the true models. The $v_{s,ver}$ model seems to be a bit more influenced by $v_{s,hor}$ than the other way round, here very weak lateral variations are visible in the model that have their origin in the true $v_{s,hor}$ model. The v_s model resulting from the isotropic inversion is in this case an almost perfect reconstruction of the true horizontal velocity model, with some artifacts in the shallow part. The density models are for both inversions similar, far from the true density model and highly influenced by the structures of $v_{s,hor}$. A look at the misfit development of both inversion shows that the misfit converges in this example much better for the VTI inversion than for the isotropic one (see figure B.2). It can be reduced more in the anisotropic case in each frequency stage, so that the final misfit is more than one order of magnitude smaller than for the isotropic inversion. This better reduction of the misfit is also correlated to a higher number of

iteration steps, compared to the isotropic inversion more than 100 additional iterations are calculated. Despite this difference of final misfit, the data fit of both inversions is quite similar, both retrieved subsurface models can almost perfectly explain the observed waveforms (see figure B.3).

The results of this synthetic test combined with those of the previous test show that structures of the subsurface can be reconstructed properly as well for the horizontal as for the vertical velocity component. An isotropic inversion of VTI data will mainly yield the horizontal velocity as v_s model, while the inverted densities are in both cases not reliable. Depending on the true subsurface models, it is possible that datafit and final misfit of isotropic FWI are as good as for the results of VTI FWI, even if the obtained v_s model does not contain any information about anisotropy. However, for other models, it can also happen that a significant improvement is attained by using a VTI inversion. It is therefore recommendable to use an anisotropic FWI when expecting a VTI subsurface, otherwise the obtained models will probably explain the data very well, but all information about anisotropy will be missing so that the v_s model gives no correct image of the subsurface.

4.3. Crosstalk test

Our previous tests already showed that the inversion for density and velocities is biased, so that the inverted density model contains structures that exist only in the true velocity models. In this section, we investigate this crosstalk between different parameters further to estimate the reliability of the inversion results.

For this synthetic test, we use spatial uncorrelated models for the three parameters $v_{s,ver}$, $v_{s,hor}$ and ρ. The models consist of a layer with gradually increasing velocities and densities over a halfspace with $v_s = 400\,\frac{\mathrm{m}}{\mathrm{s}}$ and $\rho = 2050\,\frac{\mathrm{kg}}{\mathrm{m}^3}$ starting at a depth of 10 m. Additionally, in each model a rectangular shaped anomaly is added with a value of of $v_s = 300\,\frac{\mathrm{m}}{\mathrm{s}}$ for the velocity anomalies and $\rho = 1950\,\frac{\mathrm{kg}}{\mathrm{m}^3}$ for the density anomaly. The squares have a width of 7 m and a height of 2 m and are all located in a depth of 3 m, but their horizontal position is different for each parameter (see figure 4.9). By choosing different locations of the anomalies for each model parameter, we will be able to see in the inversion results which parameters are biased the most and how strong the effects of crosstalk are. As initial models, for each model the background model without the anomaly is used. The acquisition geometry is the same as for the previous synthetic tests with 48 receivers and 10 sources equally distributed at the surface. All parameters are updated simultaneously and as before, we start the inversion for low frequencies (up to 5 Hz) and increase the frequency content step by step during the inversion.

The inversion results are shown together with the true models in figure 4.9. In both velocity models, the anomaly is clearly reconstructed at the correct location. However, the absolute values of the anomalies in the inverted models do not correspond to the true values, but are for the vertical as well as for the horizontal velocity about $50\,\frac{\mathrm{m}}{\mathrm{s}}$ to slow. The shape of the anomaly is better resolved for the vertical velocity, in the horizontal velocity model the borders of the square are more blurred but the shape is still recognizable. Regarding the crosstalk, only weak effects are visible in the velocity models. In the result for $v_{s,ver}$, weak perturbations of the background model can be seen at the right side where the $v_{s,hor}$ anomaly is located. The density anomaly shows no effects on $v_{s,ver}$. In the $v_{s,hor}$ model, the effects of the other velocity component are even smaller. The anomalies of $v_{s,ver}$ and ρ seem to have no effects on the reconstruction of the horizontal velocity. Again, supporting the results of the previous tests, the final density model shows a much worse reconstruction of the true model than the velocity models. The density anomaly in the center of the model is almost not visible, instead anomalies appear in the

inverted density model at the places where the velocity anomalies are located. Especially the $v_{s,ver}$ anomaly is clearly visible as a positive density anomaly, even its shape is reconstructed. At the location of the $v_{s,hor}$ anomaly, the background density model is strongly perturbed. It is obvious that the structures in the true velocity models have a stronger influence on the density inversion than the structures in the real density model. The strong updates in the density model at the locations of the velocity anomalies can also be a reason why the absolute values in the density models are underestimated. A higher density at those places can compensate the velocity differences between true and inverted models.

All in all, the crosstalk test showed that both velocity components are only weakly biased and almost not at all influenced by density structures. On the other hand, the density inversion is highly influenced by structures of the velocity models, so that the density model itself can not be reconstructed properly. Those different effects of crosstalk might be explained by equations (2.64) - (2.66). The density gradient depends directly from the squared horizontal and vertical velocities, while the velocity gradients are proportional to the density and to the respective velocity component, but not from the other velocity component. Therefore, the effects of density on the velocities are weaker than the other way round, and the crosstalk between the two velocities is only minimal. For the application of FWI to real data, the different biasing of the parameters has the meaning that the results for horizontal and vertical velocities can be considered to be reliable, while the density model will probably not contain any information about the true density of the subsurface, but is mainly coupled to the velocity models.

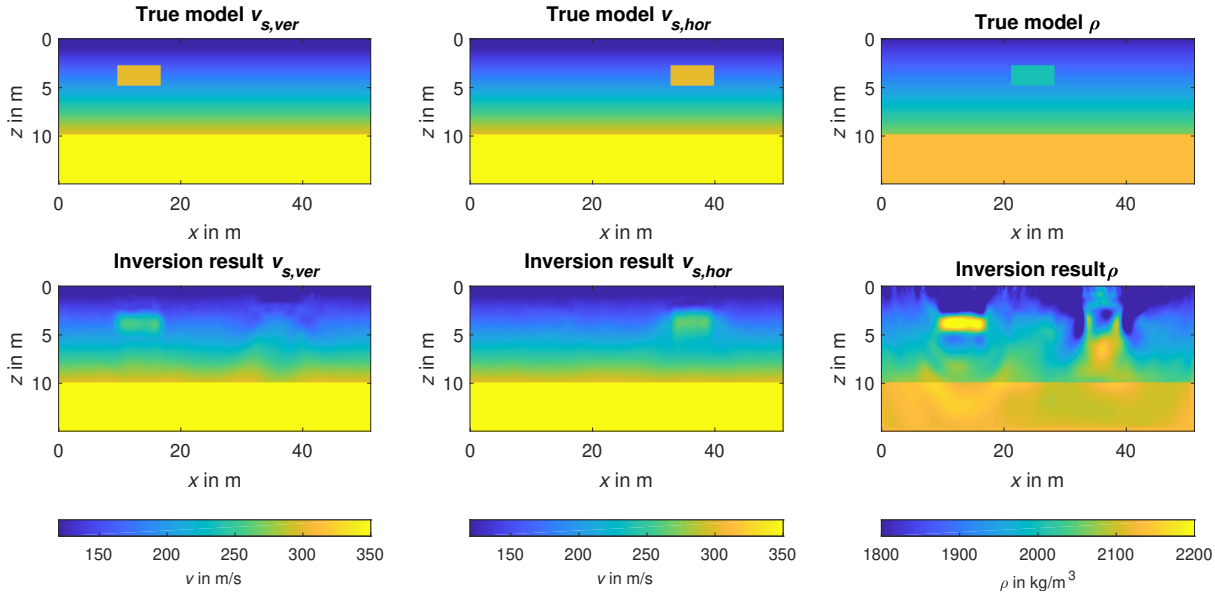

Figure 4.9.: Synthetic test for the investigation of crosstalk between vertical velocity $v_{s,ver}$, horizontal velocity $v_{s,hor}$ and density ρ: True models (top) and results of the VTI inversion (bottom).

4.4. Summary

In summary, the inversion tests presented in this chapter show that the VTI inversion of data generated in anisotropic models gives good results for synthetic data. It is possible to retrieve from VTI data the correct subsurface structures for horizontal and vertical velocities, even if the structures are spatially uncorrelated. For the deeper parts of the models, it can be problematic to resolve the correct absolute values because of the weak illumination and because of updates in the density model that compensate the errors in the velocity models. The inverted density

models showed in all tests no adequate results. It was not possible to reconstruct the true density models, instead the inversion results are strongly influenced by the two velocity models. Therefore, the results for density will in the following not be considered to be reliable. On the other hand, the inversion of both velocities is only weakly influenced by the second velocity or the density, so that even spatially uncorrelated subsurface models of those two parameters can be reconstructed properly.

One problem for the application of VTI FWI is that when applying an isotropic FWI to VTI data, it is not always possible to see directly from the results that the subsurface might have an anisotropic structure. It is possible to get a good data fit with an isotropic model, mainly because anisotropic effects are projected into the density model, and also the inverted models show no artifacts that could indicate anisotropy. Therefore, it is of advantage to know before the inversion if the subsurface at the survey site might have a VTI structure, otherwise it is not necessary to use the VTI inversion which is more expensive concerning computational resources than the isotropic inversion.

5. Inversion of field data

5.1. Setting

For a first application of the VTI FWI on real data, a test site is required where we can be sure that the subsurface has a VTI structure. Additionally, it would be ideal if the subsurface is known, so that the inversion results can be verified. Otherwise, it would not be possible to judge if the reconstructed models correspond to the true subsurface or if the data is fitted but with wrong models. Therefore, a site with a nearby geological outcrop or with a known subsurface given by other measurements or drillings would be ideal. An adequate site was found at the village Ohmden near Stuttgart.

5.1.1. Regional geology

Geographically, the region where the measurement took place belongs to the foothills of the Swabian Alb. During the Jurassic period, southern Germany and thus also the Swabian Alb was flooded by a large ocean, the Jurassic sea. The marine deposits from this time period, divided into Lower, Middle and Upper Jurassic, were consolidated with the time under the pressure of overlying materials and form today the base of the Swabian Alb. In the Alb foreland, the limestones of the Upper Jurassic and also the layers of Middle Jurassic have been removed by erosion, so that there the sediments of Lower Jurassic can be found near to the surface (see figure 5.1). The main sediment of Black Jurassic that appears in the region of Ohmden is the Posidonia shale. Although if it is from the geological definition not really a shale, but a bituminous clay marl, this sediment has a fine layered structure as a shale and is therefore assumed to be strongly anisotropic. Johnston and Christensen (1995) showed that the difference of horizontal and vertical velocities in shales can take values up to 35 %. Therefore, we expect also for the Posidonia shale a significantly higher horizontal velocity than vertical velocity.
The thickness of this shale layer lies normally between 4 m and 16 m. Because of a lack of oxygen at the bottom of the Jurassic Sea in the Black Jurassic period, the Posidonia shale contains a high number of marine fossils like ammonites, fish and marine reptiles which can be found today at a few spots in the Alb foreland where the shale lies at the surface (Geyer and Gwinner, 1968). Next to such a spot, called the Schieferbruch Kromer, our survey site is located. It is a slate quarry which can be accessed by visitors to search for fossils. The advantage of this quarry is that at its border, an outcrop of approximately 5 m height lays open, so that the structure of the subsurface can be derived from there. A photo of this outcrop is shown in figure 5.2. The upper edge of the Posidonia shale is clearly visible in a depth of about 2 m. The shale is covered by loose sandy sediments. This sediment layer can be divided from the photo into two sublayers. The first 50 cm consist of very sandy soil with a totally homogeneous structure. Below, the sediments are more consolidated and show weakly a layered structure, so that this part could also be slightly anisotropic. As we can see on the photo, the shale layers are aligned almost perfectly in the horizontal plane, which is optimal for the inversion since this horizontal layering creates an ideal VTI structure. It was possible to put a seismic profile just on top of this outcrop parallel to the border, so that the layered structure visible in the outcrop is expected as inversion result.

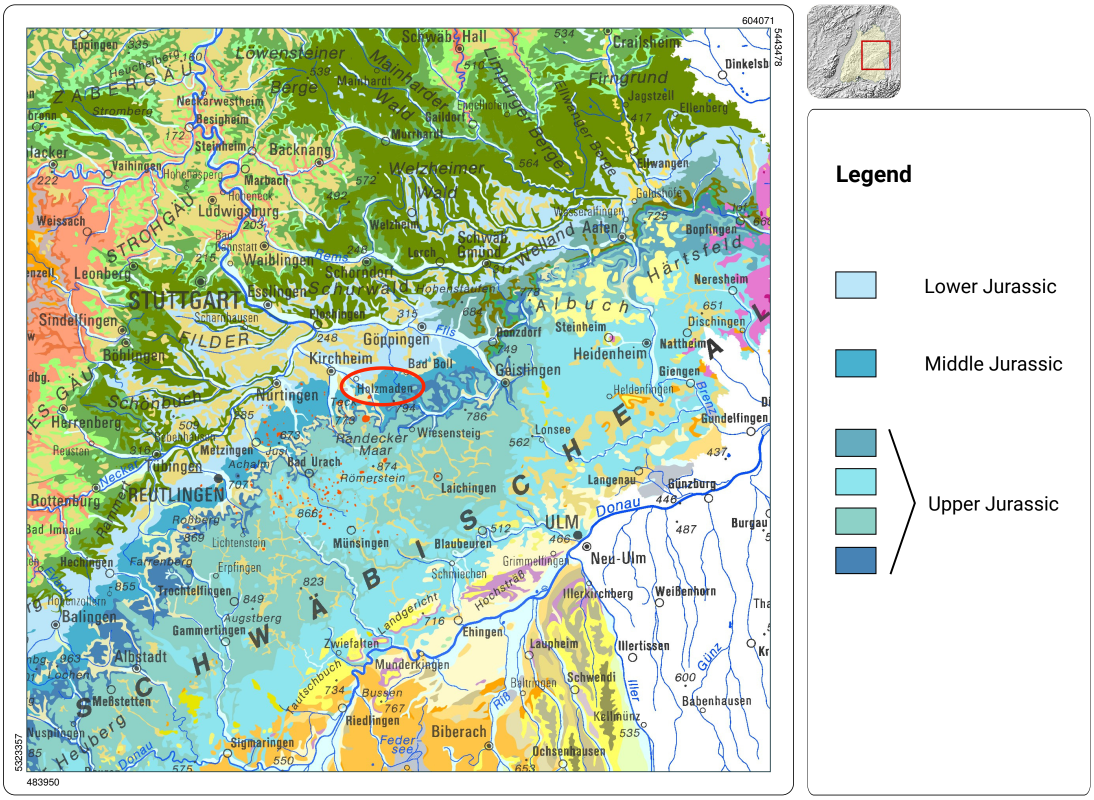

Figure 5.1.: Geological map of the region of the Swabian Alb (Landesamt für Geologie, Rohstoffe und Bergbau, 2017), with coordinates of the corners given in UTM. In the legend, only the relevant Jurassic layers are mentioned. The red circle indicates the location where the seismic measurement took place (next to the village Holzmaden).

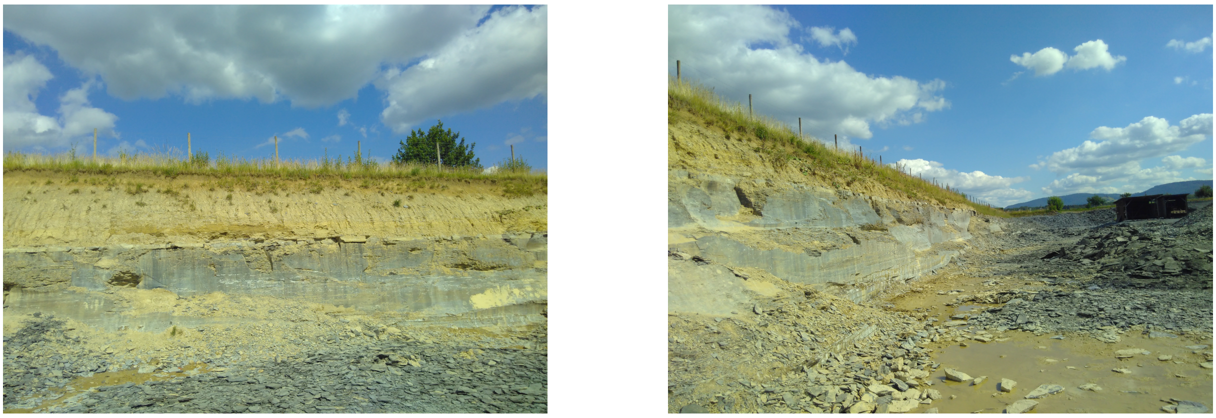

Figure 5.2.: Photos of the outcrop on top of which the seismic data was acquired. The total height of the outcrop is approximately 5 m. Clearly visible is the upper edge of the Posidonia shale in about 2 m depth.

5.1.2. Acquisition

As mentioned before, the measurement was carried out on top of the outcrop shown in figure 5.2. We measured along one single profile parallel to the break-off edge with a total length of 52 m. To avoid 3D effects from this edge in the data, the profile was set up with a distance of 5 m to the edge. We used 48 3-component geophones with an eigenfrequency of 4.5 Hz spaced with intervals of 1 m. 27 shots were executed every 2 m with the first shot located 2.5 m behind the last geophone, so that the shot positions were always inbetween two geophones. In figure 5.3, the acquisition geometry with source and receiver positions is represented schematically. We acquired SH data as well as P/SV data, even if in this work only the SH data will be analyzed. The P and SV waves were excited by vertical hammer blows on a steel plate and were recorded on the vertical component of the geophones (z). The SH waves were excited by horizontal crossline hammer blows on a steel rack and recorded on the horizontal crossline component (y). The SH shots were executed from both sides of the rack, so that the shots from the two sides can be subtracted afterwards to remove signal components with P/SV polarization. For each shot position, three single shots were stacked to enhance the signal-to-noise ratio.

Since the site was part of a golf course, the measuring conditions were optimal. The flat surface with very short cut grass and the homogeneous soil allowed an exact positioning of the geophones along a straight line with an accuracy of a few centimeters. The soil also ensures an excellent ground coupling of the geophones.

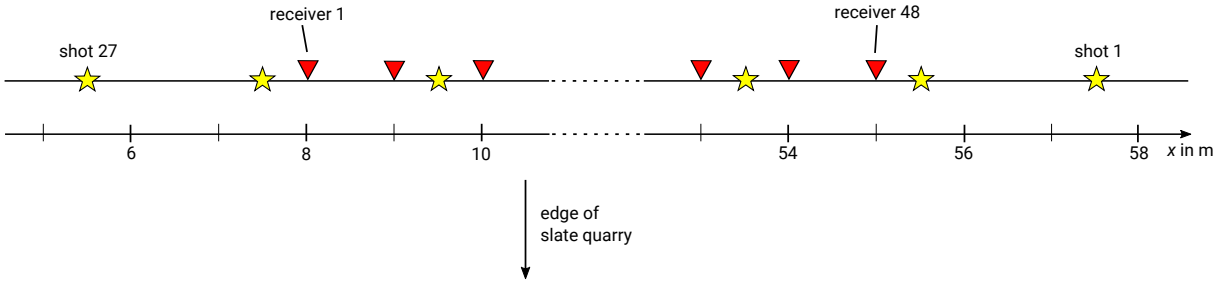

Figure 5.3.: Sketch of the acquisition geometry with positions of receivers (red triangles) and sources (stars). The x-axis is equivalent to the axis used in the following for the parameter models.

5.2. Observed data and preprocessing

The acquired data is of very high quality because of the ideal conditions given by the golf course. Still, it is necessary to do some preprocessing of the data before inverting it. In this section, we will explain the preprocessing steps that were applied on the data. In the following, we will only work with the SH data.

The first processing step is to subtract the two shots from the opposite directions at each shot position. By this, the P/SV polarized signal components that remain in the single shots are removed since they are polarized in the same manner for both shots, while the SH components are oppositely polarized so that they get enhanced by the subtraction.
The next, most important step is the 3D to 2D conversion. In a 2D simulation as we use it with IFOS2D, sources are always implicitely considered to be line sources orientated along the third, missing axis (y). However, real data is always generated in 3D, even if only one profile is used, since the waves excited by the hammer blows are propagating from these point sources in all directions. The geometrical spreading of point and line sources is different, so that real and simulated data would differ even for the true model in phases and amplitudes only because of the

line source assumption in the simulation. Trying to simulate the real data with 2D line sources will therefore introduce errors that are not caused by the subsurface model. The measured data thus has to be converted to be comparable to the 2D simulated data. We use therefore the direct wave transformation proposed by Forbriger et al. (2014), which consists of a convolution of the data with $\sqrt{t^{-1}}$ and a multiplication with $r\sqrt{2}\sqrt{t^{-1}}$, where r stands for the offset.
Next, we mute on all traces the signals recorded before the onset of the clearly visible refracted wave since we know that they are only noise that we do not want to be fitted by the inversion. Additionally, we add at the beginning of the signal 0.02 s of zeros to avoid artifacts that could be caused later by filtering or inverting of the source time function. Finally, we resample the data that was acquired with a time sampling of $\Delta t = 250\,\text{ms}$ with a new time sampling of $\Delta t = 0.04\,\text{ms}$ to guarantee a stable simulation. The original total recording time was $T = 1.5\,\text{s}$, but we clip the data now at $t = 1.1\,\text{s}$ because this time interval contains the main part of all signals. A filter is not applied to the data, since it will be filtered during the inversion and we thus avoid double filtering.

Figures 5.4 to 5.6 show the seismograms of first, last and middle shot after preprocessing. For better visualization, the seismograms are normalized tracewise. The data quality is excellent, almost no noise is visible even in the unfiltered data. Only on the traces next to the sources low-frequency noise is visible which can be easily removed with a high-pass filter. For some shots, the nearest traces are clipped because the amplitudes were too high to be registered, therefore we will mute for the inversion traces with offsets smaller than 3 m. The seismograms are dominated by the Love wave that is highly dispersive as we can see in the first and the last shot. Additionally, a refracted wave that forms the first onsets is clearly visible, its low slope indicates a layer with a high velocity as its origin. For far-offset traces, the amplitudes of the refracted wave are even higher than those of the surface wave, which is rather unusual and probably caused by high attenuation in the shallow part of the subsurface.

The frequency content of the data can be seen in figures 5.7 and 5.8. Figure 5.8 shows the averaged amplitude spectrum of all 27 shots. The main frequency content of all data lies in the range between 10 Hz and 110 Hz, with a maximum of the spectrum at about 30 Hz. High amplitudes also occur for very low frequencies, they correspond to the low-frequency noise on the near-offset traces and will be removed during the inversion with a high-pass filter, since all frequencies below the eigenfrequency of 4.5 Hz should be removed anyway. In figure 5.7, the amplitude spectra of all traces of shot 27 are plotted separately. This allows us to see the offset-dependency of the amplitude spectra and so to differentiate the frequency contents of surface and body waves. All in all, the frequencies lie between 10 Hz and 100 Hz. The spectra are wider at small offsets, probably because of more noise caused by the people that executed the hammer shots. With increasing offset, the frequencies are shifted slightly to lower frequencies. Especially for the furthest offsets, the spectra can be divided into two parts separated at 50 Hz. Differing from the traces with smaller offsets, here the amplitudes of frequencies larger than 50 Hz are as large or even larger than for lower frequencies. In the seismogram (figure 5.4), we have already noticed that the refracted wave has for large offsets higher amplitudes than the Love wave. From this observation, we come to the conclusion that the frequency part above 50 Hz corresponds to the refracted wave, while the frequencies of Love wave are mainly in the interval between 10 Hz and 50 Hz. This distinction will be helpful if we want to focus during the inversion on one single wave type.

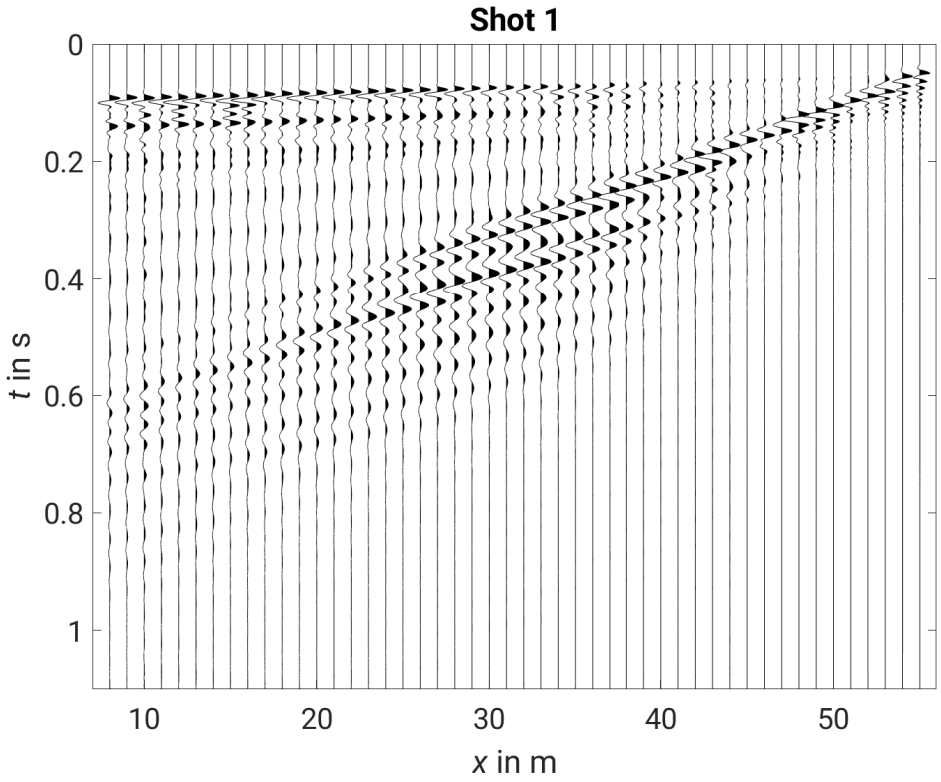

Figure 5.4.: Particle velocity v_y (SH component) from shot 1 at $x = 57.5\,\mathrm{m}$ after preprocessing. The velocities are normalized tracewise, no filter is applied.

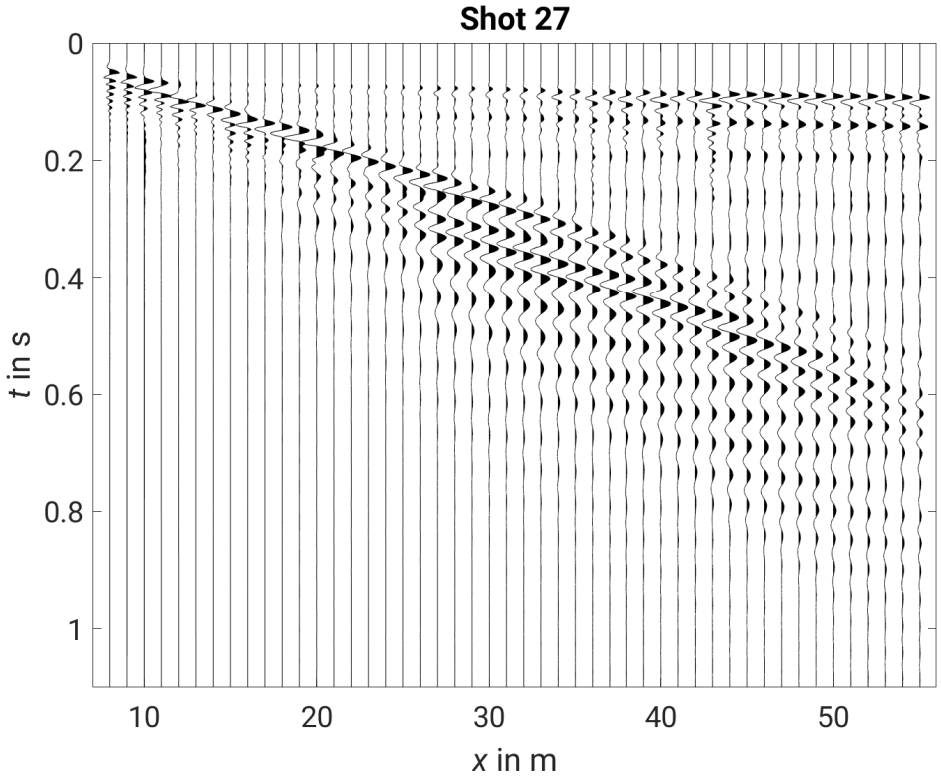

Figure 5.5.: Particle velocity v_y (SH component) from shot 27 at $x = 5.5\,\mathrm{m}$ after preprocessing. The velocities are normalized tracewise, no filter is applied.

Figure 5.6.: Particle velocity v_y (SH component) from shot 14 at $x = 31.5\,\mathrm{m}$ after preprocessing. The velocities are normalized tracewise, no filter is applied.

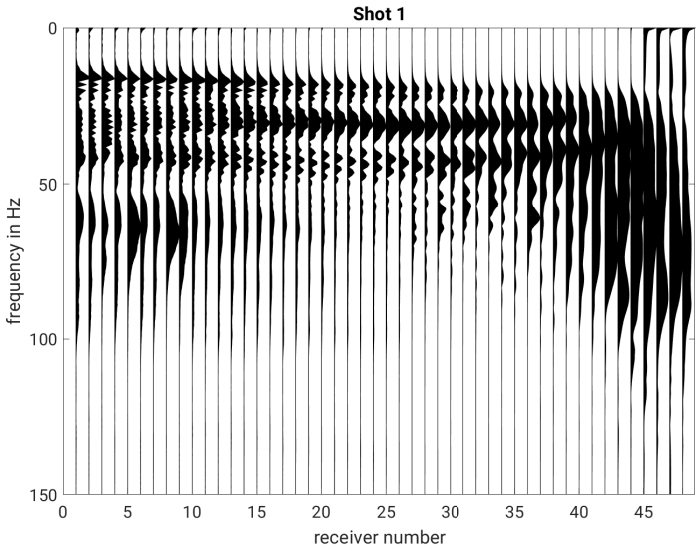

Figure 5.7.: Amplitude spectra of all traces of shot 27. The spectra are normalized tracewise.

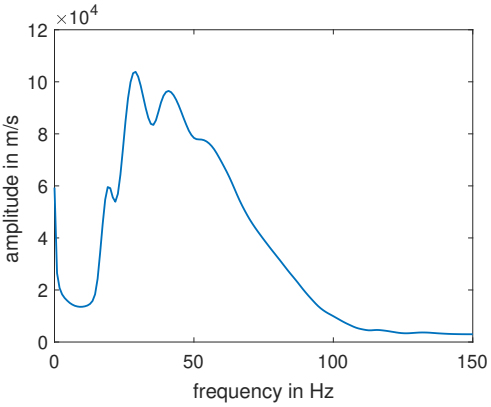

Figure 5.8.: Average amplitude spectrum of all 27 shots.

Since the wavefield in near-surface data is dominated by surface waves, we take a closer look on the dispersion curves. Figure 5.9 shows exemplarily the phase velocity spectrum of shot 27 (with the source at $x = 5.5\,\mathrm{m}$). The first mode of the Love wave can clearly be distinguished from frequencies of about 20 Hz on. For lower frequencies, the phase velocity is increasing rapidly and is because of the resolution hard do distinguish. The high phase velocities result from the high velocities of the shale, which is because of its depth only reached by the low-frequency components of the Love wave. From about 37 Hz on, a second mode of the Love wave is visible. For frequencies higher than 40 Hz, the phase velocity of the Love wave changes only slightly, it stays almost constantly at values of 120 $\frac{\mathrm{m}}{\mathrm{s}}$ to 130 $\frac{\mathrm{m}}{\mathrm{s}}$, which should correspond approximately to the velocities in the upper layer. Additionally, in this frequency range, high amplitudes occur for high phase velocities of 1000 $\frac{\mathrm{m}}{\mathrm{s}}$ to 1500 $\frac{\mathrm{m}}{\mathrm{s}}$. Those amplitudes probably correspond to the refracted wave, and the velocities thus give us a first estimation of the velocity of the Posidonia shale. The frequency range ($f > 40\,\mathrm{Hz}$) of the refracted wave also matches the observations in the amplitude spectra in figure 5.7.

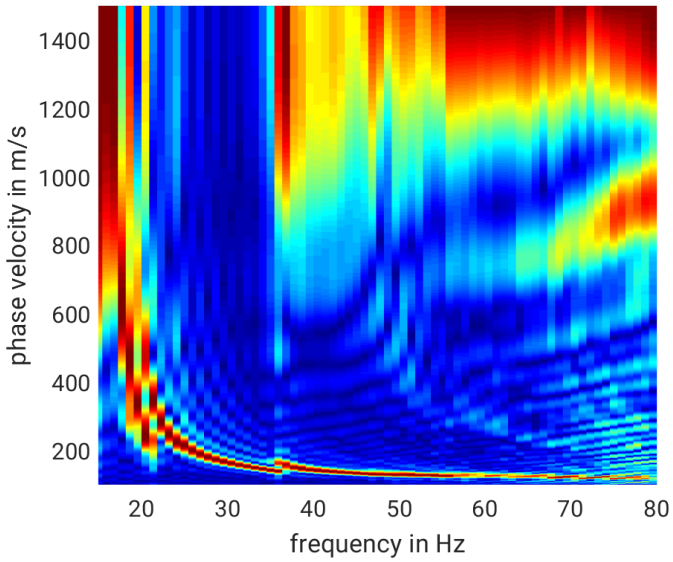

Figure 5.9.: Phase velocity spectrum of the real data of shot 27.

5.3. Inversion

5.3.1. Initial model

To derive an initial model for FWI, we make use of the information contained in the surface waves. An one-dimensional shear-wave velocity model can be derived from the inversion of the dispersion curves (Xia, 2014). For the initial model of the quality factor Q, the amplitudes of the Love wave are used to estimate the attenuation coefficients, from which the Q-values are calculated (Gao et al., 2018). The subsurface is here assumed to be isotropic, so that we will use for FWI the same initial velocity model for horizontal and vertical velocities. The resulting initial model consists of two layers over halfspace with a thickness of both layers of 1 m (see table 5.1). The first two layers have very low velocities of 108 $\frac{\mathrm{m}}{\mathrm{s}}$ and 165 $\frac{\mathrm{m}}{\mathrm{s}}$, respectively, which fits to typical velocities of loose shallow sediments. A very high contrast exists between the second layer and the halfspace which has an estimated velocity of 1500 $\frac{\mathrm{m}}{\mathrm{s}}$. This velocity belongs to the solidified Posidonia shale, from which we know from the outcrop that its top edge lies in a depth of about 2 m (see figure 5.2). For the attenuation factor Q of shear waves we get a value of $Q = 70$

in the shale layer, which can be seen as quasi elastic. In the layers above, the attenuation is much stronger with values of $Q = 7.5$ and $Q = 15$, respectively. Especially in the first layer, very high attenuation occurs, which explains why in the seismograms for far offsets the amplitudes of refracted waves are higher than those of the Love waves. Our in-situ observations also fit to this low Q-value, when installing the geophones we could see that the soil of the golf course consisted of very loose-packed sand of which we can assume a high attenuation. The strong attenuation in the shallow part makes it essential to calculate the wave propagation during FWI with the vicoelastic equations, since it can not be neglected on that scale.
The densities of the initial model are estimated from the in-situ observations and from the shear-wave velocities. For the loose sediments in the first two layers, we assume densities of 1800 $\frac{\text{kg}}{\text{m}^3}$ and 1900 $\frac{\text{kg}}{\text{m}^3}$, respectively. To the shale layer which is more consolidated, a density of 2200 $\frac{\text{kg}}{\text{m}^3}$ is assigned. Since the sensitivity of Love waves towards the density is much weaker than towards v_s, the results will not be influenced much even if the densities of the initial model are not correct, therefore this rough estimation is sufficient as initial model.

Table 5.1.: Velocities v_s, densities ρ and values of attenuation factor Q for the initial model. The values are derived from phases and amplitudes of the Love wave. z denotes the top edge of the respective layers. The velocities v_s will be used as initial values for both horizontal and vertical velocity models.

z in m	v_s in m/s	ρ in $\frac{\text{kg}}{\text{m}^3}$	Q
0	108	1800	7.5
1	165	1900	17
2	1500	2200	70

Figure 5.10 shows the observed data of shot 1 together with the data calculated in the initial model. To make both data sets better comparable, the source signal of the synthetic data was estimated by an inversion of the source time function. This is done by a method proposed by Pratt (1999) which is basically a least-squares optimization which minimizes the misfit between synthetic and real data by adjusting the source time function.

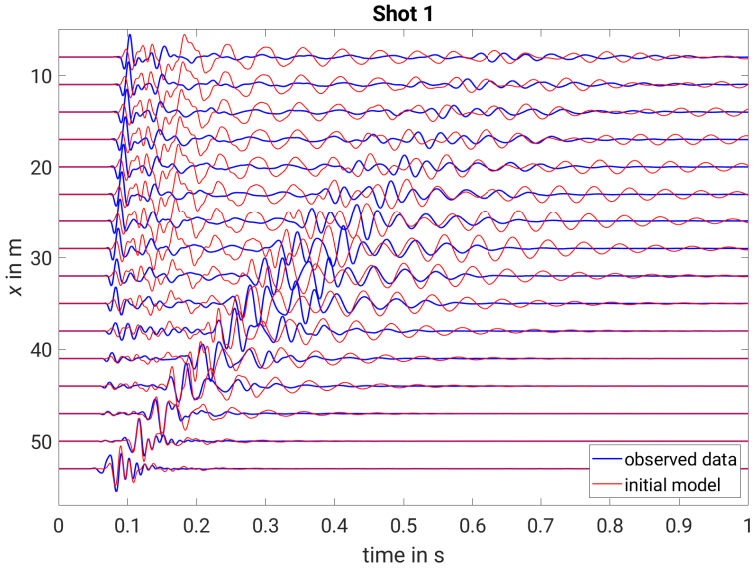

Figure 5.10.: Real data (blue) and synthetic data calculated in the initial model described in table 5.1 (red) of shot 1, located at $x = 57.5\,\text{m}$. As source signal, the inverted source time function is used. Only every third trace is displayed, all traces are normalized.

It can be seen in figure 5.10 that the initial model is already well explaining some parts of the

data. The onset times of the refracted wave fit to the real data, which means that velocity and depth of the fast shale layer are already in the correct range, but the waveforms still look very different. For the first half of the traces, the parts of the Love wave with the highest amplitudes are also similar to the real data, the fit seems there at least to be good enough to avoid cycle skipping. For the traces with higher offset, the fit becomes worse, there too high amplitudes occur directly after the refracted wave. All in all, the initial model explains the main phases and seems to be good enough to be used as starting model for FWI.

5.3.2. Inversion procedure

For the inversion, we do not use as initial model exactly the model described in the previous section. When layer interfaces are already given in the initial model, their position will only hardly be changed by the inversion, even if they are not at the correct position. Therefore, we smooth the model slightly to allow also changes of the interfaces. Figure 5.11 shows the vertical profile of the initial velocity and density models. A problem of this model lies in the high velocity contrast between the second layer and the half space. The half space, which corresponds to the shale layer, is the part of the subsurface we are most interested in, since it is there that we assume strong anisotropy. However, because of the high velocity contrast, most energy coming from the sources at the surface is reflected at this interface, so that almost no waves are penetrating into the shale layer. Consequently, the observed waveforms are mainly influenced by the parameters of the first two layers and only weakly sensitive to the shale parameters. Especially the sensitivity towards the vertical velocity is extremely weak, since almost no waves that can be registered are traveling vertically through the shale layer. Surface waves that penetrate deep enough will mainly give information about the horizontal velocity. The problems of this sensitivity is exemplarily shown in figure 5.12. We calculated the wave propagation in two different models with one of them being the isotropic model described in table 5.1. The second one is almost identical with the only difference that the shale halfspace has a differing vertical velocity of 1200 $\frac{\mathrm{m}}{\mathrm{s}}$. The difference of 300 $\frac{\mathrm{m}}{\mathrm{s}}$ between horizontal and vertical velocity, which corresponds to an anisotropy of 25 %, is quite strong but still in the range of what we expect from the Posidonia shale. The seismograms of the first shot are shown together in figure 5.12. It can be seen that the waveforms are almost identical, especially for near offsets. Small differences occur only at large offsets, but even there parts of the Love wave are still very similar. The small differences could easily be explained by other features in the model than anisotropy of the halfspace. It will therefore be very challenging to retrieve from the data information about the anisotropic halfspace.

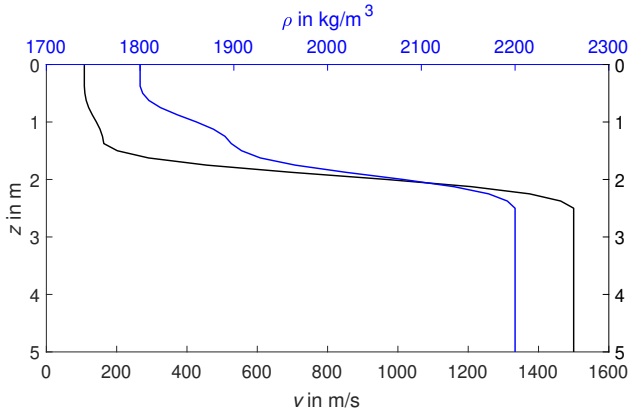

Figure 5.11.: Vertical profiles of initial velocity and density models, created by a slight smoothing of the models defined in table 5.1.

To deal with the problem of high velocity contrast, we perform two consecutive inversions. In the first one, we focus only on the upper part of the model. Because of the high contrast that is

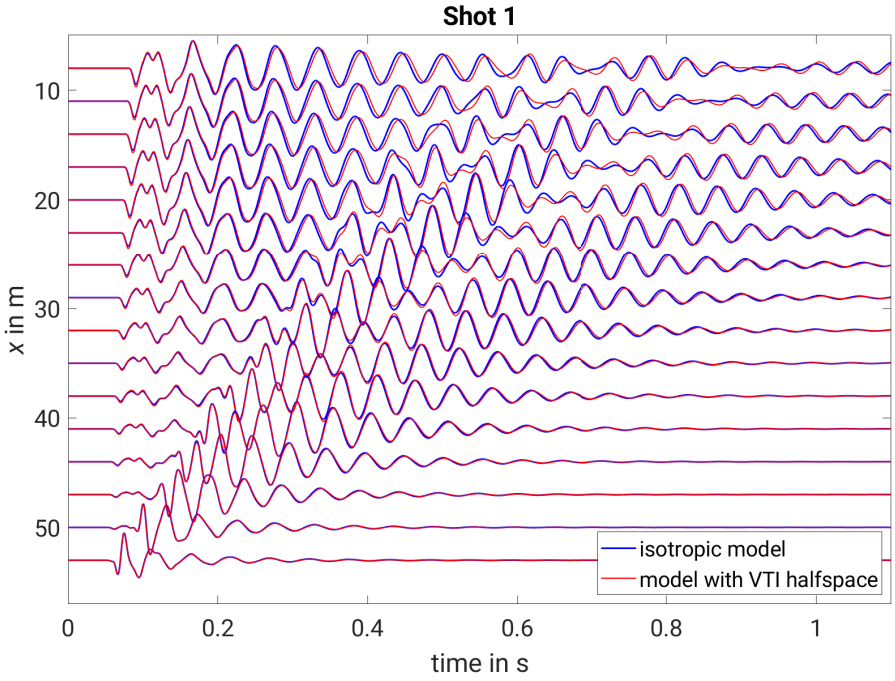

Figure 5.12.: Seismograms calculated numerically in the isotropic model described in table 5.1 (blue) and in the same model but with $v_{s,ver} = 1200\,\frac{\mathrm{m}}{\mathrm{s}}$ in the halfspace instead of $1500\,\frac{\mathrm{m}}{\mathrm{s}}$ (red). Only every third trace is displayed, all traces are normalized.

still existing in the smoothed initial model, model updates occur only above the interface at 2 m depth. The deeper parts of the model can only be modified if the shallow part is nearly correct. We use thus in a second inversion the (smoothed) result of the first inversion as initial model and apply a weighting to the gradients so that they are enhanced for the deeper model parts. Details about this procedure and the results will be shown in the next section.

The model space has a total size of 500 x 100 grid points with a grid spacing of $\Delta h = 0.125\,\mathrm{m}$. The total simulation time is 1.1 s and we use a time sampling of 0.04 ms to guarantee a stable simulation. The absorbing boundaries have on all sides a width of 10 gridpoints. As in our synthetic tests, we use a multiscale inversion and start with low frequencies to reduce the effects of cycle skipping. The data is always filtered with a high-pass with a corner frequency of 8 Hz and with an increasing low-pass filter with in the first stage a corner frequency of 12 Hz. We extend the filter in steps of 3 Hz for the first inversion, for the second one in finer steps of 2 Hz, and consider only frequencies up to 40 Hz since tests showed that using higher frequencies does not improve the inversion results. As we could see in figure 5.9, the dispersion curve of the Love wave is very flat for higher frequencies, which means that the additional information content of those frequencies is small so that we can ignore them. At the beginning of each frequency step, we invert for the source time function to reduce effects introduced by a wrong source time function. Objective function, preconditioning and other parameters are chosen equally to the synthetic tests if nothing else is mentioned.

5.3.3. Results

Figure 5.13 shows the initial models and the results for the $v_{s,ver}$, $v_{s,hor}$ and ρ models after the first inversion. Differences between initial and final models are very small and occur only in the upper first 2 m of the model. As discussed before, because of the high velocity contrast of the bedrock most energy is reflected at the interface and not propagating into the deeper part of the subsurface, so that the model is only updated in the shallow part. In the models for vertical velocity and density, we can distinguish an interface at a depth of 0.5 m to 1 m. The thickness of the top layer varies laterally, it has the highest thickness in the middle of the model and becomes thinner towards both sides. The velocity of this top layer did not change significantly compared to the initial model, which indicates that the velocity of the soil estimated from the dispersion curves was already quite accurate. Below this layer, a zone of increased vertical velocity and density is visible in the left half of the model. The result for $v_{s,hor}$ shows almost no visible differences to the initial model except from artifacts near to the surface.

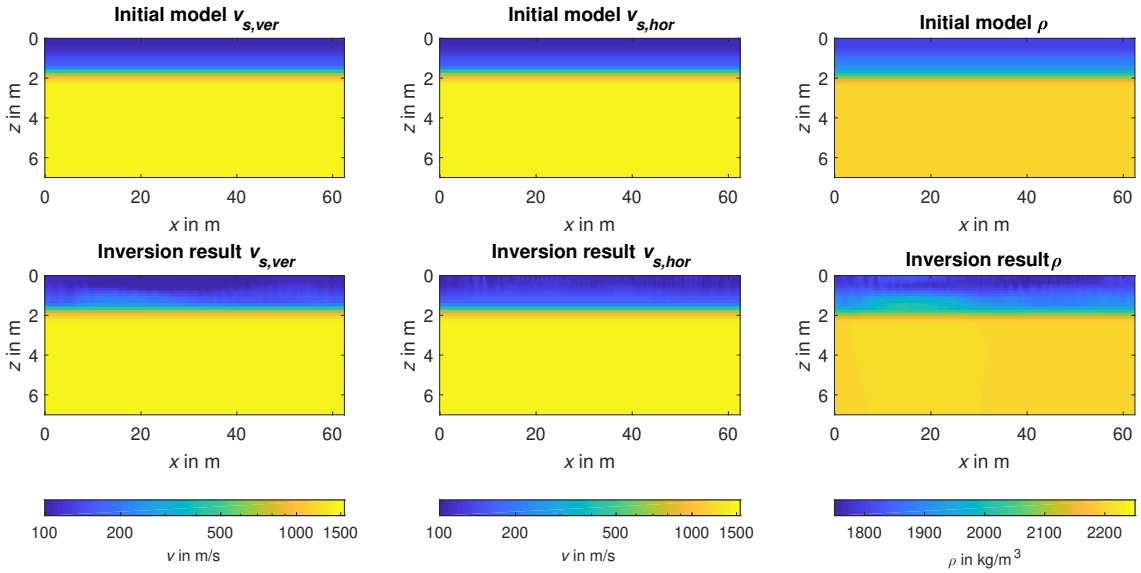

Figure 5.13.: Initial models and inversion results for vertical velocity $v_{s,ver}$, horizontal velocity $v_{s,hor}$ and density ρ at the first inversion stage.

To improve those results, a second inversion is calculated with initial models based on the previous inversion results. The models are smoothed with a horizontal gaussian filter to remove the artifacts that occur especially in the horizontal velocity model. Additionally, since we want to enhance the model updates in the deeper part, the interface at 2 m depth is smoothed stronger than before to make it possible that the position of this interface gets changed by the inversion. Therefore, we use a sinus-shaped increase of the velocity from 1.5 m to 3.75 m where the velocity of 1500 $\frac{\text{m}}{\text{s}}$ is reached.

Since we assume that the shallow part of the models got reconstructed properly by the first inversion, we allow only small updates of the parameters in this part. We multiply the gradients used to calculate the updates with a depth-dependent weighting function that suppresses updates in the upper first meter and instead amplifies the updates in greater depths. The values of those weighting factors are shown in figure 5.14. In the first meter, the gradient is multiplied with 0.1 to reduce the updates in the shallow part. For depths between 1 m and 3.75 m, the factor increases sinusoidally, and the gradients at depths greater than 3.75 m are multiplied with 50. This weighting matrix is applied to all three gradients.

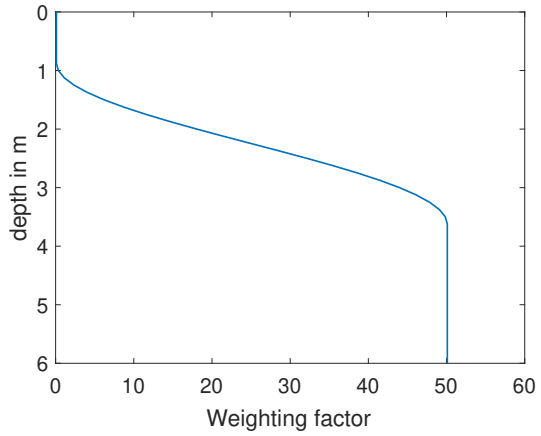

Figure 5.14.: Depth-dependent weighting function that is multiplied with the velocity and density gradients to enhance model updates in the deeper part.

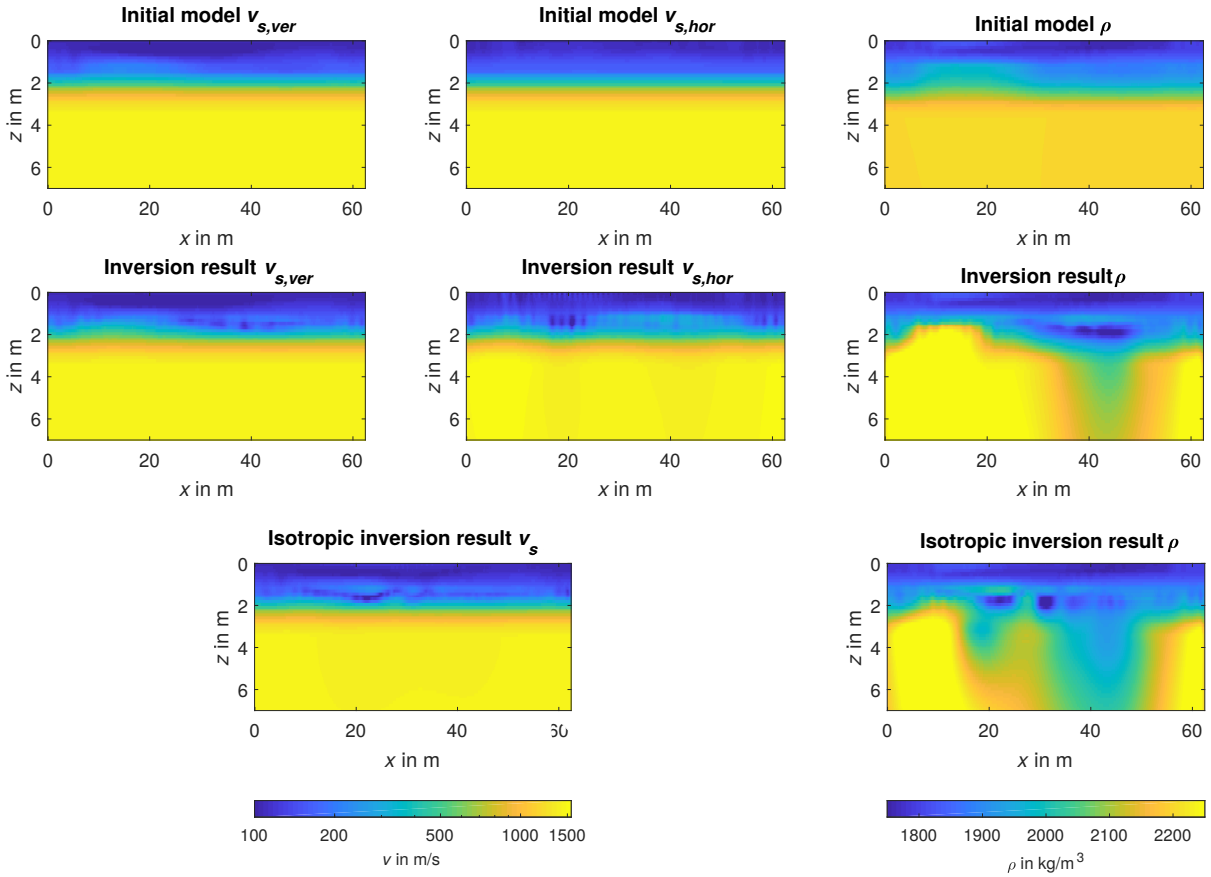

Figure 5.15.: Initial models and inversion results for vertical velocity $v_{s,ver}$, horizontal velocity $v_{s,hor}$ and density ρ at the second inversion stage. The second row shows the results of the VTI inversion, the third row the results of an isotropic inversion where as initial model the initial $v_{s,ver}$ model (first row) was used.

In figure 5.15, the initial models and the results of the second inversion are shown. Additionally to the results of the VTI FWI, we also show the results of an isotropic FWI. For the anisotropic FWI, stronger model updates appear now mainly between 1 m and 2 m depth, but below the models still do not change a lot. Only the density model shows a reduced density on the right

side over the complete depth of the model. In the velocity model, only an interface in around 1 m depth can be distinguished, but not even the top edge of the shale can be identified reliably, it can only be vaguely estimated in the $v_{s,ver}$ model. For the isotropic inversion, we used the initial model of $v_{s,ver}$ as initial v_s model. The final velocity model contains a low-velocity layer slightly above 2 m depth. It is visible along the whole profile and its depth fluctuates by maximal half a meter. The comparison with the outcrop at the test site shows that this structure could correspond to the top edge of the shale layer. Thus, the velocity near the interface and in the shale layer is not at all reconstructed properly by the isotropic inversion, but the visible velocity structure could probably indicate the location of the shale interface.

From the vertical and horizontal velocities, it is possible to calculate the Thomsen parameter γ with equation (2.3). The γ models for both inversion stages are shown in figure 5.16. In the first stage, we see clearly the interface of the bedrock at ca. 1.5 m which is caused by the initial model (see figure 5.11). Below this interface, γ remains zero since the velocities are not changed. Above, a layer with positive γ values is visible in the first 0.5 m, followed on the left side by a zone with negative γ values. The values reach from -0.2 up to 0.6 which is quite unrealistic for soil and for the sediments that had no obvious anisotropic structure. A weak anisotropy of those materials is possible, but we would expect there rather values of γ smaller than 0.1. Still, the γ model allows an identification of the interface between first and second layer. It can be assumed that the zones with different values and different sign correspond to different materials, so that we can differ from that between the soil and the sediment layer below. After the second inversion, the structures visible in the γ model are similar but slightly extended in depth. The sharp interface at the top of the shale disappeared due to the stronger smoothing of the initial model, but below 2 m γ still has values near to zero, even if in this part the strongest anisotropy is expected. In the left part of the model, the area with negative γ values just above the assumed location of the shale interface is still visible, the values became even smaller during the second inversion and reach thus values in the range of -0.5. In the same depth on the right side of the model, a positive γ anomaly occurs with values up to 0.8. Those values, as well the negative as the positive, are far too high to be realistic. They are probably caused by the fact that in this case, the Love waves are far more sensitive to the horizontal velocity than to the vertical velocity, so that updates of $v_{s,hor}$ are stronger which results in high values of γ. Especially the negative values likely do not correspond to the true model, since in shale we expect a higher horizontal velocity compared to the vertical one. A negative γ could occur if the shale is rotated so that the layering is orientated along the z-axis, but from the observations in the field this is not the case at our test site. We thus can not resolve the anisotropy of the shale properly with the used

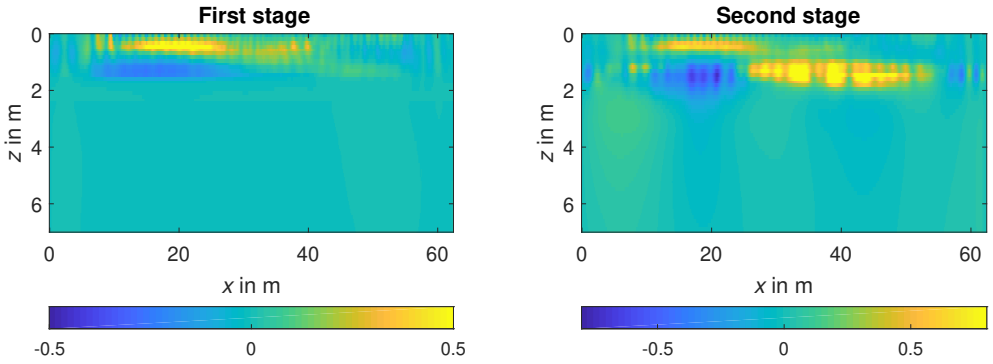

Figure 5.16.: Models of Thomsen parameter γ calculated from the vertical and horizontal velocity models after the first and the second inversion stage, respectively. Attention should be paid to the different colorbars.

method. The very high γ values could be an indication for anisotropy in the deeper model, but they do not describe the model correctly. From the inversion results, we can only estimate the top edge of the shale layer, since below no model updates occur.

To evaluate the quality of the inversion results, we compare in figure 5.17 the seismograms calculated in the final models of the second inversion stage with the observed data for the first and the last shot. The data fit of VTI and isotropic inversion is quite similar, from the seismograms it can not be seen that one of both inversion performs significantly better. This corresponds to the values of the L2 misfit that were in the same order of magnitude for both inversions. The

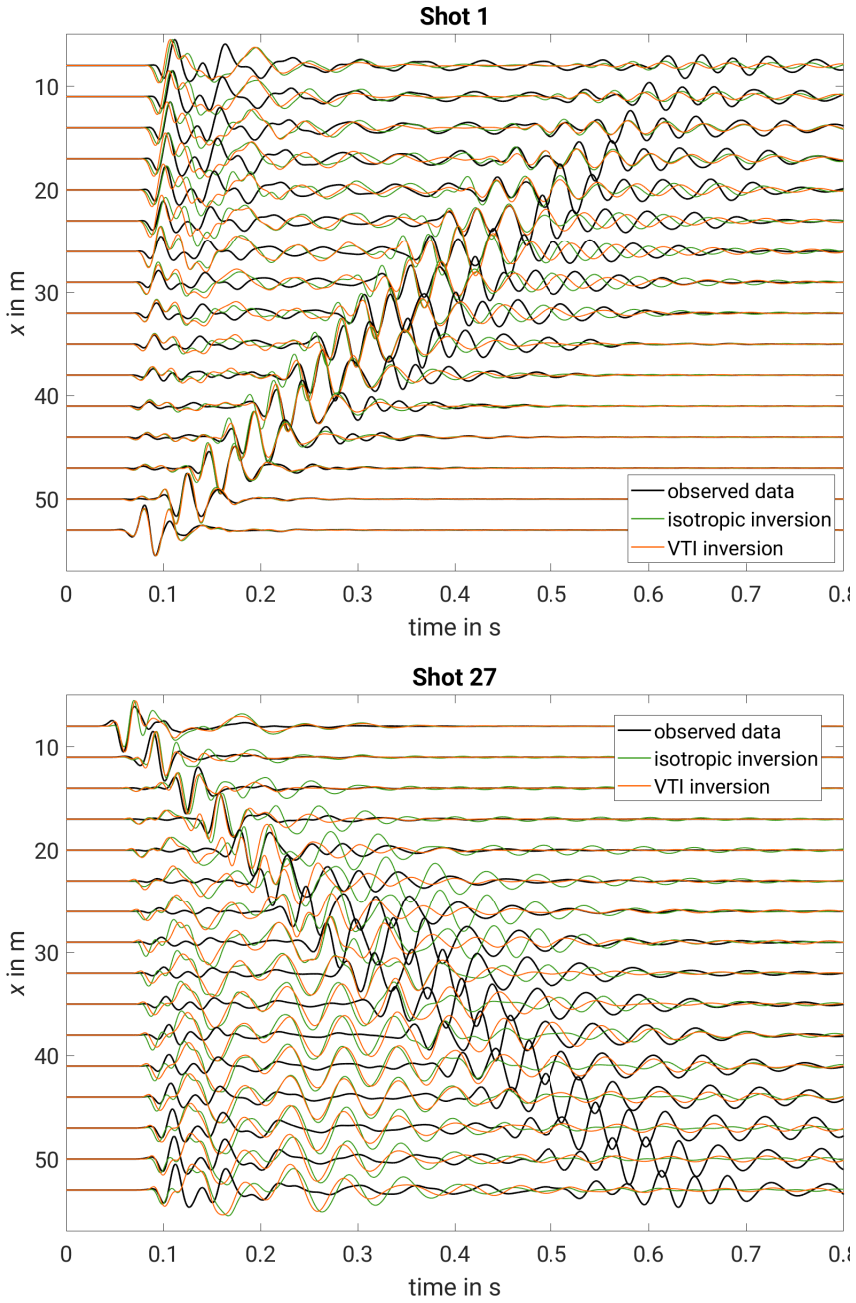

Figure 5.17.: Observed seismograms (black) filtered with a low-pass filter of 40 Hz compared with the final seismograms resulting from the isotropic (green) and VTI FWI (orange) for shot 1 and shot 27. Only every third trace is displayed, all traces are normalized.

comparison of the seismograms from the first and the last shots shows a much better data fit for shot 1 which is located at $x = 57.5\,\mathrm{m}$. There, the main phases of the Love wave and also the beginning of the refracted waves are well fitted. The fit gets worse for far offsets and for late times. On the contrary, for shot 27 (located at $x = 5.5\,\mathrm{m}$), the inverted seismograms do not really fit the observed data. Here, even the phases of the Love wave with the highest amplitudes are not fitted properly. This difference in the data fit indicates that the inverted models are better on the side of shot 1, i.e. in the right half. For the left side, which influences mostly the seismograms of shot 27, the data fit shows that the model can not correspond to the true subsurface. Thus, the part of the model with negative γ values seems not to explain the data properly, while the right side with high positive γ gives a good data fit. This matches our observations and expectations, since a negative γ is rather unrealistic at this site where the shale is lying horizontally.

All in all, it was in this case not possible to retrieve the anisotropy of the Posidonia shale properly with FWI. The inversion results show that the high velocity contrast of the bedrock is still problematic for the inversion, even if we amplify the updates in greater depths. Since we have even in the smoothed initial model a steep increase of velocities, it is difficult to enhance only the deep gradients. The smooth course of the weighting function causes a similar amplification around the interface, so that the initial strong contrast of the gradients remains almost unchanged. On the other hand, for depths further below the interface at 2 m, the strong amplification of the gradients does not compensate for the lack of information in the data. It seems that the recorded data does not contain enough information about the shale layer, since almost no waves are penetrating into this layer, and if they do they are not registered since they do not get reflected back. Another reason for the failure of the inversion could simply lie in the initial models. They are probably differing too much from the true models, so that the inversion gets stuck in a local minimum because of cycle skipping. Further reasons might lie in the handling of attenuation. We use during the whole inversion the same Q model as passive parameter for the viscoelastic forward modeling. The Q values were retrieved as 1D model from the amplitudes of the Love wave. However, it is possible and even probable that this model does not correspond to the true attenuation. To improve the results, it could be an option to invert also for Q in addition to the other three parameters. On the other hand, this additional parameter would also increase the ambiguity of the inverse problem and the computational cost, so that it can not be assured that this would really ameliorate the results.
Other options to improve the results are a different preprocessing of the data or a different inversion procedure. A separation of body and surface waves for example could make it easier to enhance model updates in the deeper part of the model. For sure the FWI workflow could also be improved, e.g. by alternating single-parameter inversions with multi-parameter inversions to compensate for the different sensitivities of the parameters. However, testing all those options would go beyond the scope of this work.

6. Conclusions

In this work, we implemented successfully the full-waveform inversion for SH waves in vertically transversely isotropic media. The inversion allows to invert simultaneously for the three model parameters density, horizontal velocity and vertical velocity. Additionally, attenuation is considered by using the quality factor Q as passive parameter, which means that the wave propagation is calculated with the viscoelastic equations for a given Q model which is not updated during the inversion. We focused in this thesis on the application of the anisotropic FWI on shallow-seismic data.

The anisotropic calculation of wave propagation was implemented with the finite-difference method and benchmarked by comparison with an analytical solution and with the isotropic forward solver. Sensitivity tests showed that a VTI structure of the subsurface has significant effects on the waveforms of both Rayleigh and Love waves, but the effects are much stronger on Love waves. Because of this higher sensitivity of Love waves, we applied FWI in this work only on the SH component of seismic waves. When dealing only with Love waves, a VTI medium can be described by three parameters, which are the density ρ, the horizontal velocity of propagation $v_{s,hor}$ and the vertical velocity $v_{s,ver}$, which is only one additional parameter compared to the isotropic case. The sensitivity tests also showed that Love waves, even if they are propagating horizontally, are sensitive to both horizontal and vertical velocities. Therefore, it should in theory be possible to reconstruct from Love waves both velocities with FWI. Those expectations were confirmed by the application of the anisotropic FWI to synthetic data. It was possible to reconstruct the models of $v_{s,hor}$ and $v_{s,ver}$ almost perfectly, even if the models were not spatially correlated. In contrast, it was not possible to retrieve the density properly with the multi-parameter FWI. An additional crosstalk test showed that the crosstalk between the two velocities is very weak or even not noticeable, while the density inversion is highly influenced by structures appearing in the velocity models, especially in the $v_{s,ver}$ model. We thus consider the density models, in contrast to the velocity models, as not reliable. A comparison of the inversion results with the results of an isotropic FWI showed that it is possible to find an isotropic model that explains the VTI data as good as the VTI model, even if we have in this case only one velocity model and thus lose all information about anisotropy. If the spatial structures of $v_{s,ver}$ and $v_{s,hor}$ are different, this will not be visible in the isotropic result, and nothing will indicate that the assumption of an isotropic subsurface is wrong. Therefore, the application of anisotropic FWI is recommended when there is a suspicion that the subsurface has a VTI structure, as an isotropic inversion would then not be able to resolve the correct models.

As a first field data application, we tried to invert data that was acquired next to a slate quarry near Stuttgart. At this site, loose sediments are overlaying the bedrock formed by Posidonia shale, which we assume to be highly anisotropic. Unfortunately, it was not possible to reconstruct with FWI the anisotropy of this shale. The main reason for this is the high velocity contrast of more than $1000\,\frac{\mathrm{m}}{\mathrm{s}}$ between the shale and the overlying materials. This causes a reflection of most wave energy at this interface, so that the recorded seismograms contain almost no information about the shale layer. Attempts to reduce this problem by weighting the model updates stronger with increasing depth did not lead to satisfying results. Another reason for the failure of the inversion is probably the consideration of attenuation only as passive parameter. An additional inversion for Q might produce better results, since the used Q model likely does

not correspond to the true attenuation.

All in all, we think that the inversion results could still be improved by the application of a different preprocessing or by a different inversion workflow. For certain, the inversion would be less problematic if the velocity contrast of different materials was smaller or if waves also got reflected at the bottom edge of an anisotropic layer. Therefore, further tests, probably also with different data sets, have to be carried out to investigate the full potential of the VTI inversion. Our synthetic tests showed the capabilities of the anisotropic FWI, and we believe that also a VTI inversion of field data is possible which will produce high-resolution models containing additional information about the anisotropic properties of the subsurface.

Bibliography

Babuska, V. and Cara, M. (1991). *Seismic Anisotropy in the Earth*. Kluwer Academic Publishers.

Backus, G. E. (1962). Long-wave elastic anisotropy produced by horizontal layering. *Journal of Geophysical Research*, 67(11):4427–4440.

Bohlen, T. (2002). Parallel 3-D viscoelastic finite difference seismic modelling. *Computers & Geosciences*, 28(8):887–899.

Bohlen, T., Kugler, S., Klein, G., and Theilen, F. (2004). 1.5D inversion of lateral variation of Scholte-wave dispersion. *Geophysics*, 69(2):330–344.

Brossier, R., Operto, S., and Virieux, J. (2009). Seismic imaging of complex onshore structures by 2D elastic frequency-domain full-waveform inversion. *Geophysics*, 74(6):WCC105–WCC118.

Bunks, C., Saleck, F. M., Zaleski, S., and Chavent, G. (1995). Multiscale seismic waveform inversion. *Geophysics*, 60(5):1457–1473.

Carcione, J. M., Kosloff, D., and Kosloff, R. (1988). Wave propagation simulation in a linear viscoelastic medium. *Geophysical Journal*, 95:597–611.

Christensen, R. (1982). *Theory of Viscoelasticity: An Introduction*. Academic Press, second edition.

Courant, R., Friedrichs, K., and Lewy, H. (1967). On the Partial Difference Equations of Mathematical Physics. *IBM Journal*, pages 215–234.

Dobry, R., Borcherdt, R. D., Crouse, C. B., Idriss, I. M., Joyner, W., Martin, G. R., Power, M. S., Rinne, E. E. E., and Seed, R. B. (2000). New Site Coefficients and Site Classification System Used in Recent Building Seismic Code Provisions. *Earthquake Spectra*, 16(1).

Dokter, E., Köhn, D., Wilken, D., Nil, D. D., and Rabbel, W. (2017). Full waveform inversion of SH- and Love-wave data in near-surface prospecting. *Geophysical Prospecting*, 65:216–236.

Fichtner, A. (2011). *Full Seismic Waveform Modelling and Inversion*. Springer Berlin Heidelberg.

Fletcher, R. and Reeves, C. M. (1964). Function minimization by conjugate gradients. *The Computer Journal*, 7:149–154.

Forbriger, T. (2003). Inversion of shallow-seismic wavefields: II. Inferring subsurface properties from wavefield transforms. *Geophys. J. Int.*, 153:735–752.

Forbriger, T., Groos, L., and Schäfer, M. (2014). Line-source simulation for shallow-seismic data. Part 1: theoretical background. *Geophys. J. Int.*, 198:1387–1404.

Gao, L., Pan, Y., Tian, G., and Xia, J. (2018). Estimating Q Factor from Multi-model Shallow-Seismic Surface Waves. *Pure and Applied Geophysics*, 175:2609–2622.

Geyer, O. F. and Gwinner, M. P. (1968). *Einführung in die Geologie von Baden-Württemberg*. E. Schweizerbart'sche Verlagsbuchhandlung, Stuttgart, second edition.

Groos, L., Schäfer, M., Forbriger, T., and Bohlen, T. (2017). Application of a complete workflow for 2D elastic full-waveform inversion to recorded shallow-seismic Rayleigh waves. *Geophysics*, 82(2):R109–R117.

Guitton, A. and Alkhalifah, T. (2017). A parameterization study for elastic VTI full-waveform inversion of hydrophone components: Synthetic and North Sea field data examples. *Geophysics*, 82(6):R299–R308.

Hestenes, M. R. and Stiefel, E. (1952). Methods of Conjugate Gradients for Solving Linear Systems. *Journal of Research of the National Bureau of Standards*, 49(6):409–436.

Johnston, J. E. and Christensen, N. I. (1995). Seismic anisotropy of shales. *Journal of Geophysical Research*, 100(B4):5991–6003.

Kamath, N., Tsvankin, I., and Díaz, E. (2017). Elastic full-waveform inversion for VTI media: A synthetic parameterization study. *Geophysics*, 82(5):C163–C174.

Köhn, D., Nil, D. D., Kurzmann, A., Przebindowska, A., and Bohlen, T. (2012). On the influence of model parametrization in elastic full waveform tomography. *Geophys. J. Int.*, 191:325–345.

Komatitsch, D. and Martin, R. (2007). An unsplit convolutional perfectly matched layer improved at grazing incidence for the seismic wave equation. *Geophysics*, 72(5).

Landesamt für Geologie, Rohstoffe und Bergbau (2017). LGRB-Kartenviewer. Regierungspräsidium Freiburg, Baden-Württemberg. `http://maps.lgrb-bw.de`. Accessed: 2018-08-13.

Levander, A. R. (1988). Fourth-order finite-difference P-SV seismograms. *Geophysics*, 53(11):1425–1436.

Liu, H.-P., Anderson, D. L., and Kanamori, H. (1976). Velocity dispersion due to anelasticity; implications for seismology and mantle composition. *Geophysical Journal of the Royal Astronomical Society*, 47:41–58.

Liu, Q. and Tromp, J. (2006). Finite-Frequency Kernels Based on Adjoint Methods. *Bulletin of the Seismological Society of America*, 96(6):2383–2397.

Moczo, P., Kristek, J., and Halada, L. (2004). *The Finite-Difference Method for Seismologists. An Introduction.* Comenius University, Bratislava.

Nocedal, J. and Wright, S. J. (2006). *Numerical Optimization.* Springer, New York, second edition.

Pan, Y., Xia, J., Xu, Y., Gao, L., and Xu, Z. (2016). Love-wave waveform inversion in time domain for shallow shear-wave velocity. *Geophysics*, 81(1):R1–R14.

Park, C. B., Miller, R. D., and Xia, J. (1999). Multichannel analysis of surface waves. *Geophysics*, 64(3):800–808.

Payton, R. G. (1983). *Elastic wave propagation in transversely isotropic media.* The Hague: Martinus Nijhoff Publishers.

Plessix, R.-E. (2006). A review of the adjoint-state method for computing the gradient of a functional with geophysical applications. *Geophys. J. Int.*, 167:495–503.

Plessix, R.-E. and Cao, Q. (2011). A parametrization study for surface seismic full waveform inversion in an acoustic vertical transversely isotropic medium. *Geophys. J. Int.*, 185:539–556.

Plessix, R.-E. and Mulder, W. A. (2004). Frequency-domain finite-difference amplitude-preserving migration. *Geophys. J. Int.*, 157:975–987.

Polak, E. and Ribière, G. (1969). Note sur la convergence de méthodes de directions conjuguées. *Revue Francaise d'Informatique et de Recherche Opérationelle*, 16(3):35–43.

Pratt, R. G. (1999). Seismic waveform inversion in the frequency domain, Part 1: Theory and verification in a physical scale model. *Geophysics*, 64(3):888–901.

Prieux, V., Brossier, R., Gholami, Y., Operto, S., Virieux, J., Barkved, O. I., and Kommedal, J. H. (2011). On the footprint of anisotropy on isotropic full waveform inversion: the Valhall case study. *Geophys. J. Int.*, 187(3):1495–1515.

Prieux, V., Brossier, R., Operto, S., and Virieux, J. (2013). Multiparameter full waveform inversion of multicomponent ocean-bottom-cable data from the Valhall field. Part 1: imaging compressional wave speed, density and attenuation. *Geophys. J. Int.*, 194:1640–1664.

Robertsson, J. O., Blanch, J. O., and Symes, W. W. (1994). Viscoelastic finite-difference modeling. *Geophysics*, 59(9):1444–1456.

Schön, J. H. (2015). *Physical Properties of Rocks*. Elsevier, second edition.

Sears, T. J., Barton, P. J., and Singh, S. C. (2010). Elastic full waveform inversion of multicomponent ocean-bottom cable seismic data: Application to Alba Field, U. K. North Sea. *Geophysics*, 75(6):R109–R119.

Socco, L. V., Foti, S., and Boiero, D. (2010). Surface-wave analysis for building near-surface velocity models - Established approaches and new perspectives. *Geophysics*, 75(5):75A83–75A102.

Tarantola, A. (1984). Inversion of seismic reflection data in the acoustic approximation. *Geophysics*, 49(8):1259–1266.

Thomsen, L. (1986). Weak elastic anisotropy. *Geophysics*, 51(10):1954–1966.

Tran, K. T., McVay, M., Faraone, M., and Horhota, D. (2013). Sinkhole detection using 2D full seismic waveform tomography. *Geophysics*, 78(5):R175–R183.

Virieux, J. (1984). SH-wave propagation in heterogeneous media: Velocity-stress finite-difference method. *Geophysics*, 49(11):1933–1957.

Virieux, J. (1986). P-SV wave propagation in heterogeneous media: Velocity-stress finite-difference method. *Geophysics*, 51(4):889–901.

Virieux, J. and Operto, S. (2009). An overview of full-waveform inversion in exploration geophysics. *Geophysics*, 74(6):WCC127–WCC152.

Warner, M., Ratcliffe, A., Nangoo, T., Morgan, J., Umpleby, A., Shah, N., Vinje, V., Stekl, I., Guasch, L., Win, C., Conroy, G., and Bertrand, A. (2013). Anisotropic 3D full-waveform inversion. *Geophysics*, 78(2):R59–R80.

Xia, J. (2014). Estimation of near-surface shear-wave velocities and quality factors using multichannel analysis of surface-wave methods. *Journal of Applied Geophysics*, 103:140–151.

Xia, J., Miller, R. D., and Park, C. B. (1999). Estimation of near-surface shear-wave velocity by inversion of Rayleigh waves. *Geophysics*, 64(3):691–700.

Appendix

A. Analytical solution

We show here the equations after Payton (1983) used in section 3.1 to calulate the analytical solution of VTI wave propagation.

The wavefronts in VTI media are defined through the x- and z-coordinates of their locations as a function of the angle θ at a certain time t. There are always two wavefronts (x_-, z_-) and (x_+, z_+) at the same time, one of the P-wave and one of the SV-wave, respectively. The equations for their analytical calculation are

$$x_\pm(\theta) = \frac{\sin\theta}{2AR_\pm}\left(2\beta\sin^2\theta + \gamma\cos^2\theta \mp \frac{\cos^2\theta(k_1\cos^2\theta - k_2\sin^2\theta)}{\sqrt{B^2-4A}}\right) \tag{.1}$$

$$z_\pm(\theta) = \frac{\cos\theta}{2AR_\pm}\left(2\alpha\cos^2\theta + \gamma\sin^2\theta \pm \frac{\sin^2\theta(k_1\cos^2\theta - k_2\sin^2\theta)}{\sqrt{B^2-4A}}\right) \tag{.2}$$

with

$$\alpha = c_{33}/c_{55} \tag{.3}$$

$$\beta = c_{11}/c_{55} \tag{.4}$$

$$\gamma = 1 + \alpha\beta - (c_{13}/c_{55}+1)^2 \tag{.5}$$

$$k_1 = 2\alpha(\beta+1) - \gamma(\alpha+1) \tag{.6}$$

$$k_2 = 2\beta(\alpha+1) - \gamma(\beta+1) \tag{.7}$$

$$\tag{.8}$$

and the functions of θ

$$A(\theta) = \alpha\cos^4\theta + \gamma\cos^2\theta\sin^2\theta + \beta\sin^4\theta \tag{.9}$$

$$B(\theta) = (\alpha+1)\cos^2\theta + (\beta+1)\sin^2\theta \tag{.10}$$

$$R_\pm(\theta) = \left(\frac{B(\theta) \pm \sqrt{B^2(\theta) - 4A(\theta)}}{2A(\theta)}\right)^{1/2} \tag{.11}$$

Additionally to the wavefronts, it is also possible to calculate the displacement for receivers located along the axis of symmetry. Due to the radiation pattern, the vertical displacement u_z can only be calculated for a vertically directed source and the horizontal displacement u_x only

for a horizontal source. We introduce four functions of $\bar{z} = t\sqrt{c_{55}/\rho}$ as

$$F_1(\bar{z}) = \left(\frac{1}{4\beta} - \frac{2\beta(\alpha - \bar{z}^2) - (\gamma - (\beta+1)\bar{z}^2)}{4\beta\sqrt{D}}\right)\left(\frac{-(\gamma - (\beta+1)\bar{z}^2) + \sqrt{D}}{-2(\alpha - \bar{z}^2)(1 - \bar{z}^2)}\right)^{1/2} \tag{.12}$$

$$F_2(\bar{z}) = \left(\frac{1}{4\beta} + \frac{2\beta(\alpha - \bar{z}^2) - (\gamma - (\beta+1)\bar{z}^2)}{4\beta\sqrt{D}}\right)\left(\frac{-(\gamma - (\beta+1)\bar{z}^2) + \sqrt{D}}{2(\alpha - \bar{z}^2)(1 - \bar{z}^2)}\right)^{1/2} \tag{.13}$$

$$G_1(\bar{z}) = \left(\frac{1}{4} - \frac{2(1 - \bar{z}^2) - (\gamma - (\beta+1)\bar{z}^2)}{4\sqrt{D}}\right)\left(\frac{-(\gamma - (\beta+1)\bar{z}^2) + \sqrt{D}}{-2(\alpha - \bar{z}^2)(1 - \bar{z}^2)}\right)^{1/2} \tag{.14}$$

$$G_2(\bar{z}) = \left(\frac{1}{4} + \frac{2(1 - \bar{z}^2) - (\gamma - (\beta+1)\bar{z}^2)}{4\sqrt{D}}\right)\left(\frac{-(\gamma - (\beta+1)\bar{z}^2) + \sqrt{D}}{2(\alpha - \bar{z}^2)(1 - \bar{z}^2)}\right)^{1/2} \tag{.15}$$

With those four functions, the Green's functions of vertical and horizontal displacement U_z and U_x can be calculated:

$$\begin{cases} \text{for } |\bar{z}| \geq \sqrt{\alpha} & U_x = 0 \quad \text{and} \quad U_z = 0 \\ \text{for } 1 \leq |\bar{z}| \leq \sqrt{\alpha} & U_x = F_1 \quad \text{and} \quad U_z = G_1 \\ \text{for } 0 \leq |\bar{z}| \leq 1 & U_x = F_1 + F_2 \quad \text{and} \quad U_z = G_1 + G_2 \end{cases} \tag{.16}$$

Those equations are only valid in this form if $(\alpha + \beta) < \gamma < (1 + \alpha\beta)$, which is the case for the parameter we use in our calculation. To calculate the displacements u_x and u_z from the Green's functions, they have to be convolved with the source signal, i.e. in our case the Ricker wavelet.

B. Synthetic tests

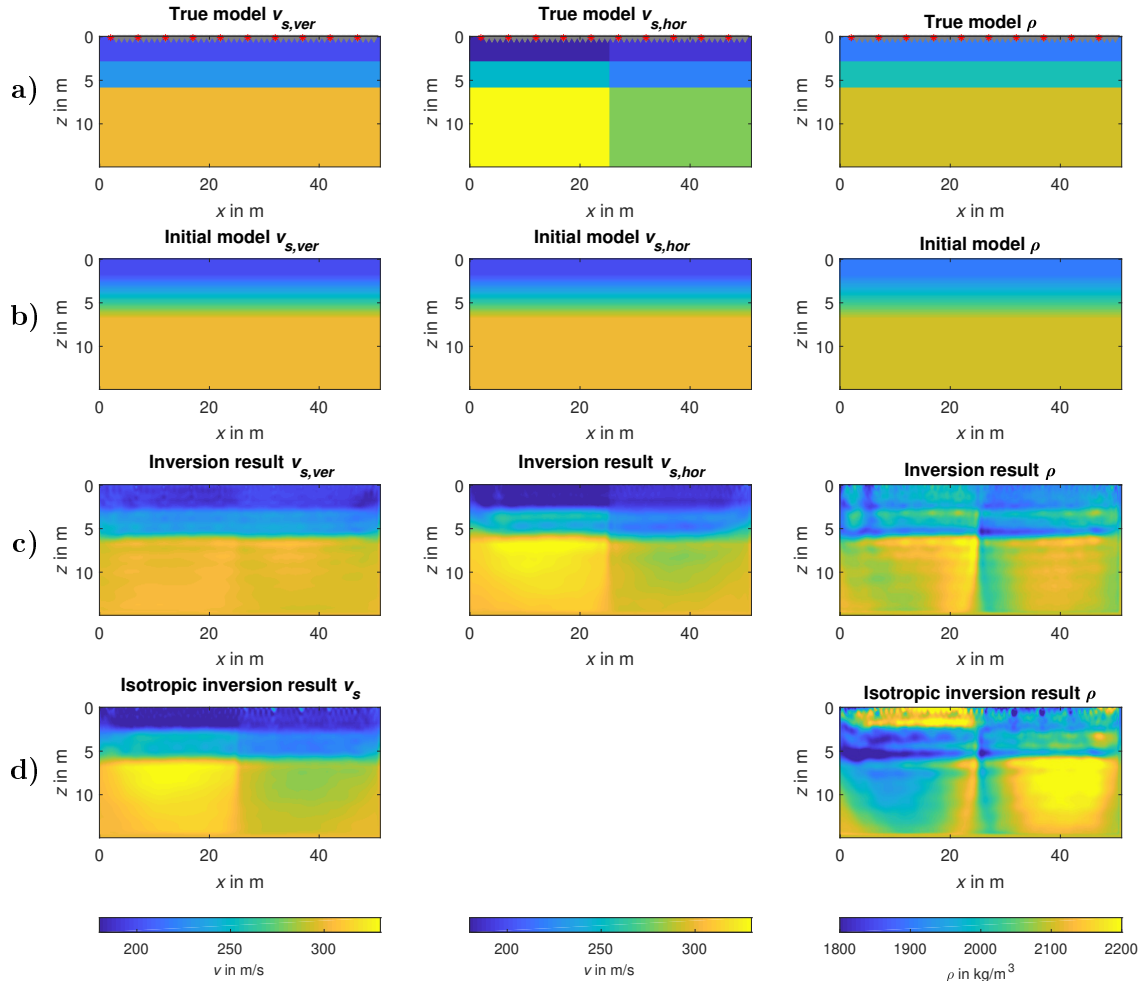

Figure B.1.: **a)** True models used to produce the pseudo-observed data. **b)** Initial models for the inversion. **c)** Results of the anisotropic FWI. **d)** Results of isotropic FWI applied on the VTI data.

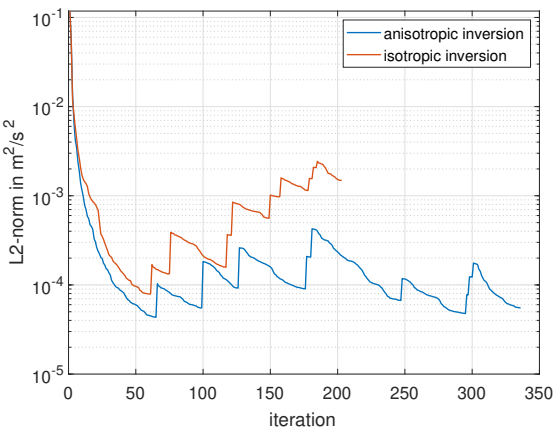

Figure B.2.: L2 misfit of VTI and isotropic FWI plotted over the number of iteration. The jumps in the misfit function correspond to increases of the frequency content of the data used for the inversion.

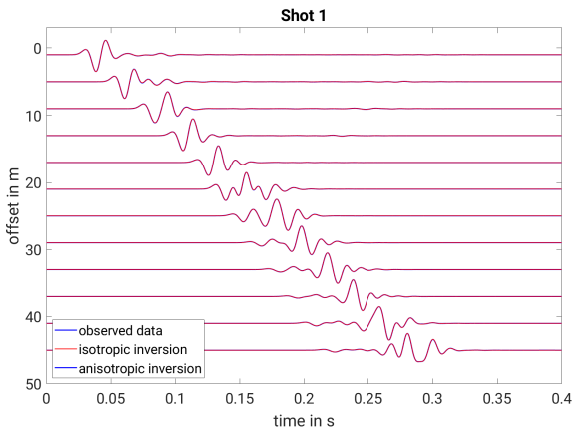

Figure B.3.: Pseudo-observed data (black) and velocity seismograms calulated in the final inverted models of anisotropic (blue) and isotropic FWI (red) for the first shot located at $x = 2\,\mathrm{m}$.

Danksagung

Zunächst möchte ich Professor Thomas Bohlen danken für den Vorschlag des Themas und für die Betreuung dieser Arbeit, sowie für viele neue Ideen und Ratschläge. Für die Übernahme des Koreferates möchte ich Professor Joachim Ritter danken. Ein großer Dank geht auch an Yudi Pan, der mich in zahlreichen Diskussionen auf neue Ideen und Ansätze gebracht hat und für alle Fragen ein offenes Ohr hatte.

Carlos Assis, Martin Pontius, Renat Shigapov und Yudi Pan danke ich außerdem für ihre tatkräftige Hilfe bei der Feldmessung, die für einen wesentlichen Bestandteil dieser Arbeit notwendig war. Auch der restlichen Arbeitsgruppe möchte ich meinen Dank aussprechen für die vielen (nicht nur wissenschaftlichen) Diskussionen, insbesondere Daniel Krieger und Fabian Kühn, die die Zeit im Büro deutlich unterhaltsamer gemacht haben. Vielen Dank auch an Claudia Payne für die Hilfe bei allen Verwaltungsangelegenheiten.

Schließlich möchte ich mich noch unter Anderem für das Korrekturlesen bei Georg Winner bedanken. Ein großer Dank geht auch an meine Eltern, die mir durch ihre ständige Unterstützung mein Studium überhaupt erst ermöglicht haben.